THESIS

THERMAL MANAGEMENT OF DISCRETIZED HEATERS USING CUW MICROCHANNEL HEAT SINKS AND FC3283 FOR LASER DIODE APPLICATIONS

Submitted by

Isabella Gascon Amyx

Department of Mechanical Engineering

In partial fulfillment of the requirements

For the Degree of Master of Science

Colorado State University

Fort Collins, Colorado

Fall 2024

Master's Committee:

Advisor: Todd M. Bandhauer

Ciprian Dumitrache
Subhas Karan Venayagamoorthy

ABSTRACT

THERMAL MANAGEMENT OF DISCRETIZED HEATERS USING CUW MICROCHANNEL HEAT SINKS AND FC3283 FOR LASER DIODE APPLICATIONS

Single-phase cooling using microchannel heat sinks (MCHS) has become a popular approach for overcoming the thermal challenges associated with high-powered microelectronic devices. Thermal management is one of the largest barriers to higher power densities in electronics and frequently limits overall device performance. The implementation of forced convective cooling via single-phase liquid cooling in MCHS reduces the thermal resistance resulting in lower device temperatures at high-power conditions, which can decrease the package size and extend the lifespan of devices. The goal of this effort was to investigate practical cooling solutions for laser diode bars. This study examined the effectiveness of a copper tungsten (CuW) microchannel heat sink paired with a dielectric coolant (FC3283) for dissipating both discrete and uniform heat fluxes up to 600 W/cm^2 across a 0.25 cm^2 surface area through a numerical and experimental study. CuW was chosen as the MCHS material because it is thermal expansion matched to GaAs, which is a common laser diode substrate. FC3283 serves as a dielectric coolant that is compatible with power electronics cooling. Reasonable agreement was found between the numerical model and the experimental results. The resulting thermal resistance ranged from 0.15 cm^2 K/W at the highest flow rate to 0.26 cm^2 K/W at the lowest flow rate. The resulting thermal performance from this study proved to be insufficient for maintaining optimal temperatures for laser diode applications. Using the validated model, cooling fluid and geometry modifications proved to have a significant impact on the heat transfer coefficients. This

study revealed the importance of considering discrete heat sources separately from uniform heat sources and proved that CuW microchannels can be a promising cooling option toward future advancements of laser diode bars and other high-power microelectronics when using a low viscosity and high thermal conductivity, dielectric cooling fluid and an optimized geometry.

ACKNOWLEDGMENTS

I would like to begin by expressing my gratitude to Dr. Todd Bandhauer for inviting me to join his team at Colorado State University and for providing guidance and advice for the past two years. My experience in this lab has taught me so much and I know it has prepared me to be successful in my future career. I would also like to offer my thanks to Dr. Charles Lewinsohn who joined the REACH CoLab during my last year at CSU and was an invaluable mentor and editor for all of my work.

I'd also like to thank the other graduate student and staff in the REACH CoLab who helped keep me sane during the challenges of graduate school. From ski trips, to our weekly taco lunches, they have made graduate school, enjoyable! Caleb Anderson has truly been one of the most helpful people throughout my graduate degree and I firmly believe I could not have completed this work without him. Maddy Siegel and Taylor Stoll have become true friends and have provided me with support that only other women in STEM can provide. And of course, Ben Platt, Fred Schmid and Victor Reyes-Flores always find a way to make me laugh when I would come upstairs for a visit. All these people and the ones I have not mentioned here, I am eternally grateful for all of you.

Finally, I would like to thank my family and friends who have supported me throughout this entire process. Moving to a new city can be extremely challenging, but I was lucky enough to have found a group of friends that made a new place feel like home. Soccer has brought me many great things, but the best thing it has always provided me with is a great community of friends. Having footy as an outlet with some of my best friends has been amazing, even after a very stressful day of failed testing or after a long day of writing. I cannot thank all my Fort

Collins footy friends enough; I am so lucky to have met you all. My family has never failed to be supportive of my education and this was no exception. Mom, Dad and Nicole (and Jacob), thank you for prioritizing visits to Colorado. I always look forward to seeing you and it has made this transition so much easier. Of course, the biggest thank you goes to my fiancée, Eric Alvarado who moved out to Colorado with me and has been my greatest support for the last two years. You have always made my darkest days, brighter and always find a way to make me smile. Thank you for being you and for joining me on this great Colorado adventure.

This work was performed under the auspices of the US Department of Energy by Lawrence Livermore National Laboratory within the LDRD program (21-SI-002)- LLNL-TH-867090

TABLE OF CONTENTS

LIST OF TABLES

LIST OF FIGURES

NOMENCLATURE

Variable	Description	Units	Formula
A	Area	m^2	
c_p	Specific heat capacity	J/kg-K	$D_h = \frac{4A_c}{PW}$
D_h	Hydraulic diameter	m	
H	Height	m	
h	Heat transfer coefficient	W/m^2-K	
$\vec{I}$	Identity matrix		
k	Thermal conductivity	W/m-K	
L	Length	m	
$\dot{m}$	Mass flow rate	kg/s	
N	Number of or finite volume	-	
ΔP	Pressure drop	kPa	
P	Pressure	kPa	
Pr	Prandtl number	-	$Pr = \frac{\mu c_p}{k}$
q''	Heat flux	W/m^2	
Q	Heat load	W	
R	Electrical resistance	Ω	
R_{th}	Area-normalized thermal resistance	cm^2 K/W	
Re	Reynolds number	-	$Re = \frac{GD_h}{\mu}$
T	Temperature	°C	
ΔT	Temperature difference between heater surface and fluid inlet temperatures	°C	
th	Thickness	m	
U	Variability	-	
$\vec{u}$	Velocity field	m/s	
V	Flow velocity	m/s	
W	Width	m	

Greek and Latin

Δ	Difference	-
δ	Uncertainty	-
ε	Radiative emissivity	-
μ	Dynamic viscosity	kPa-s
ν	Kinematic viscosity	m^2/s
ρ	Density	kg/m^3
σ	Stefan-Boltzmann constant	W/m^2-K^4

Subscripts and Superscripts

amb	Ambient
air	Air
ch	Channel
conv	Convective
f	Fin wall between channels
film	Mean air and surface temperature
h	Test section heater
i	Index in sum
in	In
out	Out
rad	Radiative

CHAPTER 1. Introduction

1.1. Motivation

Laser diode arrays have become a commonly used devices in many high-power applications. Attaining higher power densities may benefit many electronic devices such as large-scale integrated circuits, microprocessors, and laser diode arrays by improving the overall performance [2], [3]. There is a growing demand towards increasing power densities in electronics while also reducing their size which directly translates to an increasing amount of heat which must be dissipated in a small area. Current state-of-the-art is limited by the difference in thermal expansion of the materials used and thermal limitations. Advanced cooling solutions are required to achieve greater performance in laser diode arrays. Single-phase cooling in microchannel heat sinks (MCHS) is a popular cooling method for maintaining microelectronics within their optimal operating temperatures. Implementing embedded cooling techniques has been a common approach for effectively dissipating the additional excess heat from higher heat fluxes. In the past, conduction-based heat spreaders were the standard cooling option for electronics, but MCHS provides an alternative that introduces a fluid into microchannels and uses forced convection to remove heat which is a more efficient method of heat transfer than conduction [4]. Low thermal resistances can be achieved through the combination of high heat transfer coefficients, h, and using microchannels with a large surface area to volume ratio while maintaining a small hydraulic diameter [2], [3]. MCHS also allows for the cooling fluid to be integrated into the device packaging which results in improved cooling performance while preserving a small and compact package. Immersion cooling solutions for laser diode applications also requires dielectric fluid compatibility which has not been a prioritized area of research in previous studies.

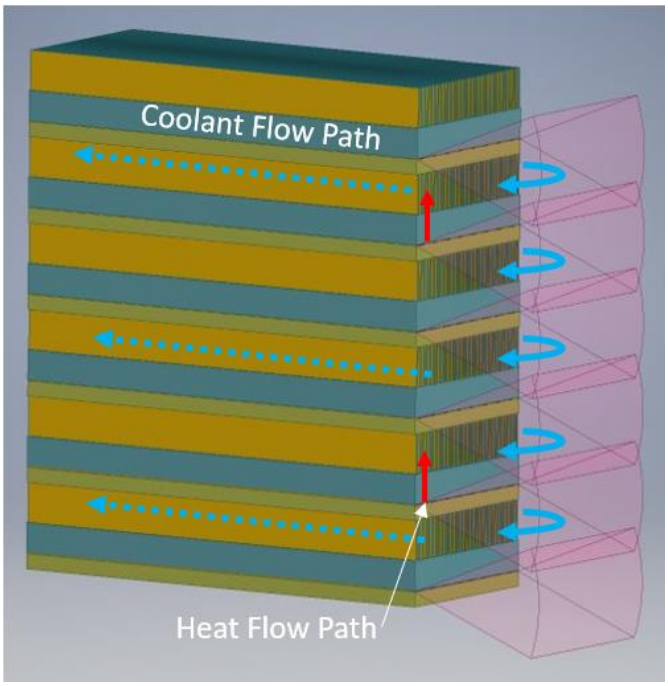

Figure 1-1- Immersion cooling design.

1.2. Laser Diode Applications

This work was motivated by the need for increasing the capabilities of laser diode arrays. Laser diodes are semiconductor devices that turn electrical work into light emitted at a specific wavelength. Many individual laser diodes can be fabricated on an internally reflected bar to emit light through a common edge, creating a laser diode bar. Current state of the art laser diode bars produce heat fluxes larger than 1 kW cm^2 on a plane parallel to the light emitting edge. Typical laser diode bars are 100mm wide, have a cavity length of 1mm and thickness of 100um [5]. By packing many laser diode bars together, one can create an array of laser diodes which can result in high brightness (light power per unit area). Increasing the brightness of laser diodes can lead to increased efficiency, decreased cost and improved lifetime and reliability. Laser diodes are unique because they are compact, have high efficiencies, tunable wavelengths, small beam waist, direct excitation with small electric currents, and have the possibility of direct modulation with applied currents. They also have low costs due to mass production and high reliability [6]. The efficiency

of laser diodes bars has increased to 50-80% in recent years, and with that, the output power has been increasing at the same rate [7].

Despite this high efficiency, there are many thermal management challenges associated with high power laser diodes. The spacing between laser diode bars in the thickness direction is known as the pitch. The combination of a small pitch and large emitted power results in a high light intensity but also requires a high required volumetric cooling rate (which in current state of the art arrays reach near 4 kW cm^3). Managing these high heat fluxes becomes increasingly difficult as the laser diode bars are packaged closer together. Forced convection is necessary to diminish the amount of heat created by the laser diodes. The maximum operational temperature of a laser diode is limited to maintaining a desired wavelength for a particular application. It is also limited to ~60°C to avoid melting adhesives used to mount micro-lenses which focus the emitted light and maintain efficient and reliable operation [5], [8]. This temperature limitation is the largest hurdle that needs to be overcome to attain higher powered laser diodes. To attain higher thermal loads and increase the lifetime and reliability of laser diode bars, improved cooling methods need to be developed and thermal expansion-matched packages need to be introduced [7].

Any high-power laser could benefit from the addition of high power-laser diodes. Some of the current laser diose applications include industrial applications, such as metal cutting, defense applications, and nuclear fusion. Laser diodes can be used for pumping laser gain media. Currently, flash lamps are most used as pumping laser gain media but they only convert ~1% of their operating power into light usable by laser gain media (e.g., Nd:YAG lasers) [6]. Laser diodes could replace the flashlamps resulting in less losses through the optical equipment currently used to amplify laser light used in achieving inertial confinement nuclear fusion.

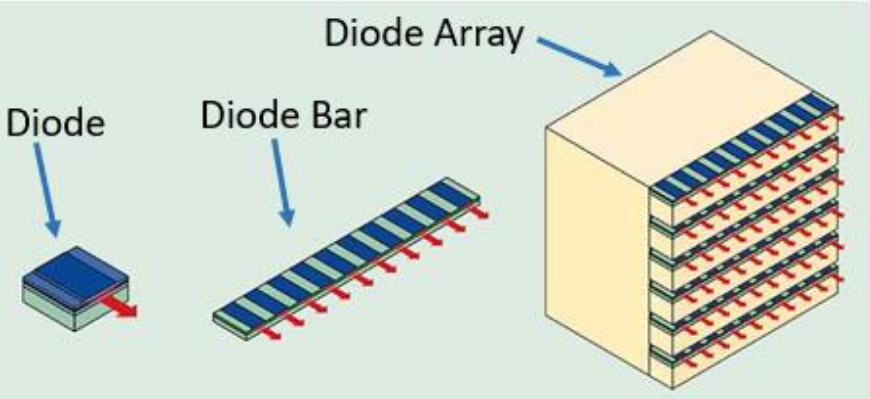

Figure 1-2- Schematic of a singular laser diode, laser diode bar and laser diode array [8].

1.3. Research Objectives

The goal of this study is to investigate practical cooling solutions for laser diode applications. As previously mentioned, there are many benefits to enabling higher power lasers but the largest constraint of achieving greater brightness in laser diodes is thermal management. Immersion cooling has been a common solution to mitigate brightness constraints. To utilize immersion cooling for laser diodes, a dielectric fluid must be used to be compatible with cooling power electronics, which lead to the selection of FC3283. In efforts of reducing thermal stress, copper tungsten (CuW) was selected as the microchannel material due to the thermal expansion compatibility with gallium arsenide, a common laser diode substrate. This study will investigate cooling several different heater designs, representative of typical laser diode bar profiles, using the unique combination of CuW and FC3283. This cooling solution provides a direct and practical solution for laser diode applications.

1.4. Thesis Organization

The following chapters details the experimental and simulation study of CuW microchannels with FC3283 for cooling surrogate laser diode heaters. Chapter 2 of the document will provide a literature review of the available and relevant studies on previous experimental,

numerical and analytical investigations regarding microchannel coolers. Chapter 3 will discuss the testing methods used in this work including the experimental set up and process. Chapter 4 will cover the modeling approach for creating a simulation for validating the experimental results. Chapter 5 will present the results from the experimental work and compare it to the model predictions. The final chapter will provide closing remarks and offer recommendations for future work.

CHAPTER 2. Literature Review

The present study will focus on single-phase cooling of high heat flux electronics using copper tungsten (CuW) microchannel coolers and FC3283 as the cooling fluid. This chapter will review the previous studies that are relevant to this work. There are many different cooling methods in addition to single-phase liquid cooling that are commercially available or under current investigation such as air cooling, gas cooling, jet impingement cooling and phase transition cooling. This paper will cover liquid cooling in rectangular microchannel heat exchangers, but a brief description of flow boiling will be included in this section as it is another common microchannel cooling method currently being researched. This overview of all the relevant work aims to provide context for the current study. In the sections below, a review is provided on the relevant literature on previous numerical, experimental, and analytical studies that focused on single-phase liquid cooling using microchannel coolers. Following the review of literature, the primary research gap will be identified, and the specific aims of this study will be presented.

2.1. Background

The effectiveness of a cooling technology or method is often defined by its thermal resistance which is a measure of a material's resistance to heat flow. Thermal resistance is defined in Equation (1):

$$R_{th} = \frac{\Delta T}{Q} = \frac{T_h - T_{in}}{Q} \tag{1}$$

where ΔT is the temperature rise of circuit or heater above the inlet cooling temperature and Q is the total dissipated power. Materials with higher thermal resistances act as insulators. When considering a system, the total thermal resistance is the sum of all the independent thermal resistances throughout the system. For a heat sink, the total thermal resistance is a sum of the

thermal resistance due to conduction (conduction through substrate material, packaging, and heat sink interface), thermal resistance due to convection between the heat sink and fluid and thermal resistance due to the sensible heating of the fluid as it absorbs energy passing through the heat exchanger [2]. Each of these independent thermal resistances should be minimized to achieve the lowest possible thermal resistance.

One of the main impediments of obtaining a low thermal resistance is the convective heat transfer coefficient, h, which is a measure of how easily heat is transferred between two mediums (for example, a solid material and a fluid). Heat transfer coefficient is defined in Equation (2):

$$h = \frac{q}{\Delta T} \tag{2}$$

where q is the heat flux and ΔT is the temperature difference between the solid surface and the cooling fluid. The heat transfer coefficient is a property that varies depending on the specific conditions of an interface. A higher the heat transfer coefficient implies more efficient and effective heat transfer in a system. For heat sinks using single-phase laminar flow, the heat transfer coefficient scales inversely with channel width which means microscopic channels result in a higher heat transfer coefficient. Using channels with high aspect ratios has also become a common practice to increase the convective heat transfer area. A high aspect ratio refers to the ratio of the channel width to its height. A high aspect ratio will further reduce the thermal resistance which is what has resulted in the tall and thin microchannel heat sinks that are commonly used today [2].

MCHS can be made using many different substrate materials and can vary in geometries. Additionally, the cooling fluid used within the microchannels also can vary. These variables are chosen based on the specific application. Using materials with high thermal conductivities is incredibly important in attaining good thermal performance through a low thermal resistance, but there are many other factors that can affect the heat transfer coefficients. In general, smaller

microchannels have better thermal performance due to a higher surface area exposed to the cooling fluid but smaller microchannels can also result in higher pressure drops. Different cooling fluids have different thermal properties and different viscosities which can have a large impact on the thermal performance and on the pressure drop. All of these must be considered when selecting materials and designing MCHS.

Traditional MCHS consist of rectangular microchannels with varying height and width, but microchannels can take many different shapes and designs. As previously discussed, the geometry of the microchannels can have a strong effect on the effectiveness of the MCHS. Geometry can also impact the flow regime of the fluid within the channels. Different flow regimes can significantly impact the heat transfer performance due to changes in velocity profiles and turbulence levels. The three flow regimes commonly observed in microchannels are laminar flow, transitional flow and turbulence flow. Laminar flow is typically smooth and orderly movement of fluid and turbulent flow is chaotic fluid flow. Turbulent flow regimes often produce higher heat transfer rates due to the enhanced mixing from the eddies forming in the fluid but can result in the consequence of higher pressure drop. The Reynolds number is a dimensionless value that predicts flow behavior and is defined in Equation (3):

$$Re = \frac{\rho V L}{\mu} \tag{3}$$

where ρ is the density of the fluid, V is flow velocity, L is the characteristic length or hydraulic diameter for microchannels, and μ is the dynamic viscosity of the fluid. The laminar regime is generally observed at Re < 2000, the transitional regime is typically seen at approximately 2000 < Re < 4000, and the turbulent regime generally occurs at Re > 4000. These values can vary depending on the specific system and geometry. It is also important to consider external factors that can impact the flow within the channels such as surface roughness and manifold design. It has

been found that the manifold design can have a substantial impact on flow uniformity which can greatly impact the effectiveness of microchannel cooling [9].

2.2. Proof of Concept Studies

The concept of microchannel heat sinks was introduced by Tuckerman and Pease [2] in 1981. This initial study used silicon (Si) MCHS with rectangular channels to successfully dissipate a heat flux of 790 W/cm2 over a 1 × 1 cm^2 heater footprint with water. The rectangular channels were approximately 50 µm wide and 300 µm deep. During their testing, the maximum temperature rise experienced by the substrate was 71°C above the fluid inlet temperature on 23°C, which resulted in a maximum thermal resistance of 0.09 cm^2 °C/W over the 1 cm^2 area. Since then, MCHS has been recognized as an enabling technology for high heat flux dissipation on the order of 1 kW/cm^2 [10]. The work of Tuckerman and Pease launched several analytical, numerical, and experimental studies looking to optimize the performance of MCHS. There have been many studies that investigate the optimized geometry of microchannel coolers, some of which will be discussed below [10-21]. Additionally, many of the studies discussed in this chapter focused on further investigating single-phase cooling using silicon microchannels and water [1], [7], [10], [11], [22], [23].

As previously mentioned, laser diodes could benefit tremendously from the integration of MCHS. Several studies have focused on the applications of MCHS to laser diode arrays. L. J. Missaggia et al. [24] successfully demonstrated cooling a two-dimensional continuous-wave (cw) laser diode array using a Si MCHS and water. This paper reports the first application of MCHS for cooling a two-dimensional laser diode array. The laser diode array used in this study was 1 x 4 mm^2. The laser diode array consisted of 41 rows of lasers with 4 in each row, row spacing was ~ 100 µm and row length ~1.02 mm. The array area was significantly smaller than the area of the

heat sink (0.04 cm^2 vs 0.8 cm^2). During this experiment, the laser diode operated with 1.33 W of CW optical output power (32 W/cm^2) with an average heat dissipation of 500W/cm^2 which is noted to be an unusually inefficient array. This study operated with a pressure of ~ 482 kPa at a flow rate of 2 x 10^{-5} m^3/s (max pressure 517 kPa). The average Reynolds number was approximately 2000 which is near the transition between laminar and turbulent flow regimes. They found a resulting in a thermal resistance of 0.04 cm^2 K/W and was extrapolated to find a thermal resistance of 0.07 cm^2 K/W for a 1 cm^2 heated area. It was found that the use of the heat sinks provided a significant increase in the optical performance of the laser diode array (output optical power) and the experimental data was in good agreement previous numerical studies.

J. A. Skidmore et al. [8] used a similar approach in their study, also utilizing a Si MCHS and water. They bonded several commercially supplied laser diode bars to a monolithic substrate while ensuring the bars were thermally isolated from one another. Microchannels were wet-etched into silicon wafers and anodically bonded to a machined glass block. The microchannels used in this study were roughly 28 µm wide on a 60 µm pitch. The laser diode was tested under continuous wave conditions with an inlet temperature of 10°C, a pressure of 50 psi and a flow rate of 45 x 10^{-6} m^3/s. This approach was found to have a lower thermal resistance and accurate bar placement improved output collimation and reduced assembly costs. Skidmore et al. were successful in achieving 1.5 kW/cm^2 at an emission wavelength of approximately 808nm and a supply limit of 165A. They found the cw thermal resistance of the 10-bar diode array to be 0.031 cm^2 K/W.

Roy et al. [25] performed a similar study using water as the cooling fluid but the microchannels were fabricated from copper instead of silicon and found similar results in thermal resistance. This study looked at a variety of laser diode test sections with the goal of reaching a heat flux of 1000 W/cm^2 over a minimum area of 1 cm^2 at an operating temperature of 300K and

a linear heat load of 100 W/cm. At the time of this study, the primary constraint of the available technology was meeting the high heat flux of 1000W/cm^2. The operating conditions for this experimental study had flow rates ranging from 6.3 x 10^{-5} m^3/s to 3.2 x 10^{-4} m^3/s and the heat fluxes ranging from 20 W/cm^2 to 650 W/cm^2. The experimental results showed a thermal resistance of less than 0.03 cm^2 K/W. This is 2-3 times better than current state-of-the-art heat sinks. An additional heat sink was tested and shown to be capable of dissipating 200-300 W of power while limiting the surface temperature rise to 20-30°C. This design also had results comparable to existing state-of-the-art heat sinks when operating at low pressures.

2.3. Experimental Studies

In addition to the experimental work performed on laser diodes, many studies have focused primarily of the cooling performance of high heat fluxes which can act as a surrogate laser diode bar or any other high heat flux electronic device. Several papers have focused their efforts on reviewing previous work in this area [26-34]. This section will discuss previous experimental studies on microchannel heat sinks. The first portion will focus on work that studied silicon or silicon carbide MCHS using water as the cooling fluid followed by the work that used other materials and fluids.

2.3.1. Si or SiC and Water

There have been many numerical and experimental studies performed on the specific combination of Si MCHS and water in addition to the studies performed by Missaggia and Skidmore. Unlike Missaggia and Skidmore, these studies used a general heat source instead of using a laser diode bar. These studies focused their efforts on the cooling performance of any high heat flux source. The key results from the literature covering the experimental testing of silicon

MCHS using water is summarized in Table 2-1 but some of the key findings and studies are discussed in further detail below.

Table 2-1- Literature Review of Single-Phase Water-Cooled Si or SiC MCHS

Authors	D_h (µm)	AR	W_{ch} (µm)	q" (W/cm^2)	Q (W)	Material	Fluid	R_{th} (cm^2 K/W)	Study
Tuckerman and Pease [2]	85.7	6.0	50	790	790	Si	water	0.09	Experiment
L. J. Missaggia et al. [24]	160	4	100	500	20	Si	water	0.0445	Experiment
R. Zhang et al. [10]	76	<6.9	44	1000	963	Si	water	0.071	Experiment
Buja et al. [22]	50	<11.6	30	600	150	Si	water	0.097	Experiment
Skidmore et al. [8]	54	27	28	1500	1500	Si	water	0.031	Experiment
Colgan et al. [13]	96/106	2.8/2.4	65/75	300	900	Si	water	0.105	Experiment
Harms et al. [35]	400	4	251	64	400	Si	water	0.2	Experiment
P.S. Lee and J. C. Ho [36]	86.3	4	54	109	109	Si	water	0.34-0.1	Experiment
Pijnenburg et al. [37]	150	3	100	428	428	Si	water	0.08	Experimental and Theoretical
L. Zhang et al. [11]	53	5	30	200	50	Si	water	0.09	Experiment/CFD simulation
Weaver et al. [4]	55	0.833	60	2000	40	SiC	water	~0.04	Experiment/CFD simulation
Cassada et al. [38]	90.5	8.0	51	1000	250	SiC	water	0.026	Experiment/CFD simulation
Cassada et al. [38]	54.3	14.3	29	1000	250	SiC	water	0.022	Experiment/CFD simulation

Harms et al. [35] reported on the experimental findings of testing a single microchannel cooler and multiple channel system. Both systems were identical except for the number of microchannels, channels were 1000 µm deep and the projected area was 2.5 cm x 2.5 cm. These are the deepest etched microchannels according to past literature at the point of publishing this paper. The intention of the deep channels was for enhanced heat transfer area. Testing conditions had Reynolds numbers from 173 to 12900. The multiple channel system was intended for laminar flow while the single channel was intended to experience turbulent flow. The results of this study

showed that the multiple channel system outperformed the single channel. While there has been an extensive amount of research regarding microchannel cooling, there is still conflicting results across the many studies, especially regarding heat transfer performance results compared to classical theories in both laminar and turbulent regimes. Some of the literature discussed in this chapter observed unique flow characteristics and thermal behavior at unexpected Reynolds number suggesting conflicting results across many studies and the need for improved correlations to accurately predict developing or turbulent flows [35], [37], [39-43].

Rahman [44] performed experimental tests of several test sections. Two main test sections were examined: parallel plates (microchannels) and a series channel (one long winding channel). Both test sections were tested with varying channel depth. Flow rate, temperature and pressure were measured at various points to calculate the Nusselt number and coefficient of friction. The Reynolds number was determined from non-dimensional analysis from the experimental data and then the Nusselt number and coefficient of friction were both plotted against the Reynolds number. Results showed that the average Nusselt number increased with the Reynolds number and there is no clear transition from laminar flow to turbulent flow at Re = 2300. The study found that the wall roughness had a more significant impact on the heat transfer than the conventional forced convection due to the small channels. This surface roughness causes a break in the development of the boundary layer along the channel wall which results in a larger rate of heat transfer to the fluid from the wall. Surface roughness is a s significant factor that can affect heat transfer and must be take into consideration in these studies.

P. S. Lee et al. [36] also reported on their results from testing rectangular microchannels with single-phase water. The flow rates ranged from 5×10^{-7} m^3/s to 1×10^{-5} m^3/s. Pressure drop and thermal resistance were measured during testing and the friction factor and Nusselt number

are also presented here. This paper's goal was to test mainly in the laminar region, but there is some discussion about the ambiguity of where the laminar region becomes transitional. The resulting thermal resistances observed in this study ranged from 0.10 to 0.34 cm^2 K/W. They were able to reach a heat flux of 109 W/cm^2 while maintaining a pressure drop of 55 kPa and a bulk fluid temperature rise of 38.4°C. This was found to be superior results to those previously seen in literature. This low thermal resistance was seen at the expense of a very high pressure drop which is due to the thick channel walls and shallow depth. For laminar flow there is an inverse relationship between thermal resistance and pressure drop. The experimental results are in good agreement with theoretical predictions and the differences can be attributed to the uncertainty when determining the pressure drop within the manifold. Manifold design is another significant factor that must be taken into consideration due to the impact it can have on the flow within the channel.

Pijnenburg et al. [37] investigated the cooling of a 1 x 1 cm^2 heater device experimentally and theoretically. They were successful in dissipating 370 W without exceeding 120°C at a flow rate of 1.67 x 10^{-6} m^3/s and a pressure drop of 15 kPa. Thermal resistance was measured throughout the test and the minimum thermal resistance was found to be 0.08 cm^2 K/W for a dissipation of 428 W and a flow rate of 1.8 x 10^{-5} m^3/s. When plotting the measured thermal resistance against the tested flow rates, they were able to see the onset of turbulence at the higher flow rates where the measured values begin to deviate from the analytical model values. The analysis assumed a fully developed flow at the entrance of the channels which is not always the case. This resulted in a lower thermal resistance experimentally. They also simulated the experiment in Flotherm which does not make this assumption and results were in better agreement with the experimental results. The paper states that the further optimization could be done by making the channels and fins

smaller and that the transition from laminar to turbulent occurred at Re = 630 which is far lower than what is typically expected in classic flow dynamics.

Colgan et al [13] studied the practical implementation of silicon microchannels for high power density chips. The channels used in this study had a 100 µm pitch and a channel width of either 65 µm or 75 µm ("narrow" vs "wide"). The goal of this study was to find optimized channel geometries. The unit thermal resistance was found to be 0.105 cm^2 K/W from the cooler surface to the inlet water and this was demonstrated with a fluid pressure drop of <35 kPa. They found that this design should be successful in cooling chips with average power densities of 400W/cm^2 or more.

R. Zhang et al. [10] replicated the study done by Tuckerman and Pease [2] and compared the repeated results to several variations of geometry including an optimized geometry. The channel geometries ranged from 50 µm wide to 334 µm wide and the optimized design was based on the first-order model developed in Hodes et al. [45]. The heat flux was applied over a 9.8 mm^2 footprint and every test section used silicon microchannels. R. Zhang et al. successfully reproduced the thermal resistance of 0.09 K/W as reported in Tuckerman and Pease and achieved a higher heat flux of 835 W/cm^2. Additionally, they found that the optimized geometry, using larger aspect ratio channels, was able to dissipate a maximum heat flux of 1003 W/cm^2 lowering the thermal resistance to 0.071 cm^2 K/W, a 21% reduction in thermal resistance. Optimizing the channel geometry is critical in these studies as it clearly has a tremendous impact on the heat transfer in microchannels.

There are many different types of microchannels such as rectangular microchannels, circular microchannels, trapezoidal microchannels, etc. Unless stated otherwise, all of the MCHS discussed so far are rectangular, parallel plate MCHS. Xia et al. [23] performed and experimental

and numerical study to compare the heat transfer characteristics and flow behavior of rectangular microchannel heat sinks (RMCHS) and staggered complex corrugated channel (CMCHS). The experiment gathered temperature and pressure drop data observed in both heat sinks and measured the average heater temperature using two methods. The first method was placing the test section in a convection oven with a calibrated thermocouple attached to the heater and measuring the heater temperature and resistance across a range of temperatures in the convection oven. The temperature and resistance data were fit to a linear polynomial in order to extract the average heater temperature. The second method was using a IR thermograph for measuring average heater temperature. A numerical simulation was used to understand and interpret the complex thermal behavior by presenting the flow field in the current complex corrugation microchannel heat sink. The simulation results, experimental results and theory were all withing 3.5% deviation of each other for the average heater film temperature. They found that CMCHS had better cooling performance compared to the RMCHS (improved heat transfer characteristics and lower thermal resistance) and a more uniform temperature distribution but experienced a much higher pressure drop.

L. Zhang et al. [11] designed and fabricated a 5 mm^2 silicon based thermal test chip with 32 µm wide and 160 µm deep silicon microchannels that were fabricated using micromachining processes compatible Si fabrication. Test sections were tested at a variety of heat loads using flow rates ranging from 4.2 x 10^{-6} m^3/s to 1.25 x 10^{-6} m^3/s. This resulted in a lower thermal resistance of 0.09 cm^2 K/W at the pumping power of about 2 W. This experimental data was compared to CFD models using ANSYS FLUENT and they reported the simulation and experimental thermal resistances to be within 10% error. One year later Buja et al. [22] designed three different Si microchannel geometries using analytical and numerical simulations and effectively dissipated a

power density of 600 W/cm^2 over a 5 mm^2 area. They found thermal resistance of 0.1 cm^2 K/W at 1 W of pumping power and 0.09 cm^2 K/W at 2 W pumping power.

As seen in the previous studies, MCHS are commonly fabricated from silicon because it is widely available and inexpensive, but previously in our group, silicon carbide (SiC) MCHS were tested to determine whether silicon carbide could provide benefits relative to silicon due to the higher thermal conductivity of silicon carbide. Cassada et al. [38], investigated SiC microchannels to remove heat fluxes up to 1 kW/cm^2 over a 0.25 cm^2 footprint with deionized (DI) water. Two geometries (50 µm and 30 µm nominally wide channels) were tested with flow rates ranging from 0.15 kg/min to 0.75 kg/min. A low thermal resistance of 0.024 cm^2 K/W was achieved at a heat flux of 1 kW/cm^2 and flow rate of 0.450 kg/min in the 30 µm wide channels. This is compared to a thermal resistance of 0.026 cm^2 K/W in the 50 µm wide channels at the same heat flux and flow rate of 0.750 kg/min. The lower thermal resistance was attained by utilizing channels with smaller hydraulic diameter (54.3µm) and higher aspect ratio (14.3). In the 30 µm wide channels, the maximum pressure drop was 72.13 psi at a flow rate of 0.450 kg/min compared to a maximum pressure drop of 38.32 psi at a flow rate of 0.750 kg/min in the 50 µm wide channels. The study concluded that similar thermal resistances can be found in larger channels at higher flow rates without the consequence of high pressure drops in the channels. The experimental values found were in good agreement with simulation results in COMSOL. The <7% difference between simulation results and experimental results was found to be partly due to broken channels that occurred during testing [38]. In addition to the work done by Cassada et al., previous work had proved SiC to be very difficult to machine due to brittleness, low fracture toughness and high hardness [4], [46].

2.3.2. Other Materials

In addition to the abundance of experimental work performed on silicon MCHS using water, there have also been several studies researching the performance of MCHS made of varying materials such as Copper or Aluminum, using a variety of fluids. The key results from the literature covering the experimental testing of MCHS using alternate materials is summarized in Table 2-2 but some of the key findings and studies are discussed in further detail below.

Table 2-2- Literature Review of Single-Phase Cooled MCHS

Authors	D_h (µm)	AR	W_{ch} (µm)	q" (W/cm^2)	Q (W)	Material	Fluid	R_{th} (cm^2 K/W)	Study
Roy et al. [25]	706	2.4	500	1000	1000	Cu	water	0.03	Experiment
Prasher et al. [47]	99.6/ 106.5 /225	4.46 /4.5 /0.6	300/65/61	1250	70	Si	Antifreeze	N/S	Experiment
Xie et al. [42]	540	9	300	86	N/S	Cu	Water/ Ethanol and FC-72	0.47 - 1.05	Experiment
H. Y. Zhang et al. [48]	380.0	9.5	210	95-136	102-189	Aluminum	Water	0.63-0.44	Experiment
Qu et al. [3]	349	3.1	231	100-200	N/S	Oxygen Free Cu	water	0.2 - 0.3	Experiment/ CFD simulation
Mandrusiak et al. [12]	100	1	100	N/S	N/S	SiC	50-50 propylene glycol water mixture	N/S	Experiment/ CFD simulation
Calame et al. [49]	737.0	2.8	500	1000-4000	N/S	OFHC Copper, AlN, Si, polycrystalline CVD SiC	water	0.02-0.025	Experiment/ CFD simulation
Raghuraman et al. [14]	247	4.7	150	N/S	100	Cu	water	N/S	Experiment/ CFD simulation

Nayak et al. [50] designed a thermal module for efficiently dissipating high heat loads using a liquid coolant and forced convection through copper microchannels. This study reports on a 3 x 3 array of 1 x 1 cm^2 Si thermal chips which are constructed on a 5.4 x 5.4 cm substrate with microchannels underneath. Both turbulent and laminar conditions were investigated but the water

flow rate was scaled to keep the linear water velocity the same for the deep and shallow channels for comparison. The module was designed for thermal dissipation up to 40 W/chip while maintaining a max operating temp of 40°C with an inlet coolant temp of 20°C. For the deep channels, the results showed a temperature rise of 18°C for a power dissipation of 42 W/chip and flow rate of 12.6 x 10^{-5} m^3/s, and for the shallow channels, the temperature rise was 19°C for a power dissipation of 42W/chip at a flow rate of 1.9 x 10^{-5} m^3/s. In addition to the experimental testing of the Cu MCHS, Nayak et al. also performed simulations using different substrate materials to compare to the performance of Cu. It was found that in the simulations using SiC, Si, and Al_2O_3, for 40W dissipation, the temperature rise on the chip was 1°C, 3°C and 12°C higher, respectively, compared to Cu. While these were promising results for Cu MCHS, which are easier to fabricate than Si, the main concern is the large mismatch between the coefficient of thermal expansion between Cu and Si.

P. S. Lee et al. [39] performed an experimental investigation of several Cu test sections with Reynolds numbers varying from 300 to 3500 and hydraulic diameters ranging from 318-903um. The focus of this paper is to examine the validation of conventional correlations and numerical analysis approach in heat transfer behavior in MCHS and matching inlet and BCs. They used pressurized nitrogen gas instead of a pump to provide a steady flow. Flow rates ranged from 1.7 x 10^{-6} m^3/s to 3.7 x 10^{-5} m^3/s. FLUENT was used for computational analysis and numerical predictions for comparison and found their experimental results to be within 5% of numerical predictions when the boundary conditions were carefully matched. They found that decreasing the channel size resulted in an increase in heat transfer coefficient at a given flow rate. Results also showed that a simplified thin wall model was able to accurately predict the heat transfer

performance but, for the developing and turbulent conditions, improved correlations are needed to account for the developing conditions.

Xie et al. [42] experimentally investigated the single-phase heat transfer of two different fluids: FC72 and a 30% ethanol-water solution. Experimental results were then compared to previous literature and analysis were carried out to determine the influences of liquid velocity, super cooled temperature, microchannel structures, and the wall temperature, etc. on heat transfer behaviors. The correlations of flow resistance and heat transfer characteristics are provided for the water-ethanol solution and for the FC 72 solution. The results from experimental testing showed that the transition from laminar to turbulent conditions occurred at Reynolds number ranging from 750-1250 for FC 72 which is significantly lower than classical theory. The experiments indicated that the convective heat transfer performance of the ethanol-water solution was superior to FC 72. They found that the heat transfer and flow behaviors in rectangular microchannels are highly dependent on the type of coolant and the geometric configuration of the channels.

H. Y. Zhang [48] studied the convective cooling of two different ball grid array (BGA) packages (12 mm x 12 mm and 10 mm x 10 mm) using an aluminum heat sink and water. The microchannels use a thermal interface material to reduce the contact thermal resistance at the interface. The measured thermal resistances observed ranged from 0.63 to 0.46 cm^2 K/W for the 12 mm chip and 0.59 to 0.44 cm^2 K/W for the 10 mm chip (due to the higher heat spreading resistance at the heat sink base). In addition to the experimental testing, an analytical study, which took the simultaneous developing flow into consideration, was also performed to predict the pressure drop and thermal resistance which they found to be in good agreement with the experimental results.

Calame et al. [49] investigated a wide variety of microchannel materials and configurations using water as the cooling fluid, allowing a comparison of performance and the resulting GaN temperatures. In this testing, an AlGaN/GaN heterostructure operated as a direct current resistor which created a localized heat source. This heat source was sized to represent power amplifiers. The microchannel coolers were cut using a diamond slitting saw, 7 channels were cut, each were approximately 500 μm wide by 1.4 mm tall, with a center-to-center pitch spacing of 1.0 mm. Silicon and AlN microchannel coolers exhibited good thermal performance at lower power densities (1000–1200 W/cm^2 over 3 x 5 mm^2 to 2 x 5 mm^2 active areas). The Polycrystalline chemical vapor deposited (CVD) SiC MCHS was found to be the most promising, especially at higher power densities (3000–4000 W/cm^2) where the 1.2 x 5 mm^2 active areas experienced a 120°C temperature. A hybrid microchannel cooler made of low-cost CVD diamond on polycrystalline CVD SiC was also tested and exhibited moderately better performance (20–30%) than the polycrystalline CVD SiC alone.

2.3.3. Flow Behavior in Microchannels

As previously discussed, the flow behavior in microchannels has a significant impact on the heat transfer performance. This includes behaviors such as flow regime, flow distribution and the impacts of surface roughness. Many studies have focused primarily on researching the impacts of these effects. Liu D. et al. [40] performed experiments on microchannels with hydraulic diameters ranging from 244 to 974 μm at Reynolds numbers from 230-6500. 8 different test sections were tested (4 long and 4 short) at flow rates ranging from 1.3 x 10^{-6} m^3/s to 1.7 x 10^{-5} m^3/s. The experiment measured the pressure drop across the channels and then compared the values to numerical predictions. The position of the pressure ports changed depending on the length of the channels. Flow visualization, using a dye entrained into the flow upstream of the

microchannels and a color video system within a video inspection microscope, confirmed the onset of turbulence at Re = 2202 in the wider channels. This onset of turbulence in the long channels was confirmed by the friction factors which started to deviate from the laminar predictions at around Re = 2000, indicated the flow entering the transition phase. The results show that conventional theory was successful in predicting the flow behavior in the channels studied in this paper. Although there are general guidelines that map out the different flow regimes, the reality is that there are many factors that contribute to the onset of turbulence so there is no true theoretical limit for transition occurring at a specific critical Reynolds number. In fact, some of the studies discussed here observed transition to turbulent conditions at significantly lower Reynolds numbers than classical theory predicts [37], [42].

Siva et al. [51] performed experimental work to study how flow maldistribution can affect temperature distribution in microchannels. In this experimental work, the hydraulic diameter and channel flow configuration was changed, along with varying chip power loads to observe the effect on pressure drop and temperature distribution across the parallel channels. This study had 3 variations in channels size which they classify as “microchannels” (88 μm), “transition to microchannels” (176 μm) and “macrochannels” (352 μm). The results showed that there was less flow maldistribution in smaller channels because of the increase in pressure drop in each channel which resulted in a reduced average and peak temperature of the test section. Additionally, higher heat fluxes resulted in a reduced viscosity which consequently increased the flow maldistribution. Flow maldistribution is another important consideration when designing microchannels and the manifolds.

Liu Y et al. [41] investigated the flow behavior and heat transfer characteristics due to surface roughness. Six test sections were fabricated with various roughness (relative roughness

ranged from 0.58% to 1.26%) out of stainless steel. Each test section had 30 microchannels with the width and depth being 0.4 mm. Experiments were conducted with Reynolds numbers ranging from 200-2100 and the friction factor, Nusselt number, heat transfer coefficient, and thermal performance were analyzed based on the experimental results. The results showed a remarkable effect on the performance of flow behavior and heat transfer due to varying surface roughness. As the surface roughness increased, the heat transfer in the microchannels increased. The Nusselt number and friction factor increased with increasing relative surface roughness. The results also indicate that the heat flux rarely affects the Nusselt number. They concluded that flow resistance in the channels increases as the surface roughness increased and that the effect of surface roughness on the heat transfer characteristics cannot be neglected, especially at high Reynolds numbers due to its effect on the thermal boundary layer.

2.4. Numerical Studies

A large portion of the literature available has focused primarily on numerical and analytical studies of MCHS. The following section will provide a review of the key numerical and analytical studies performed on MCHS. Numerical studies offer additional in-depth insights that may not be observable with experimental studies, but they usually need grounding in experimental studies for validation purposes. Following the early work of Tuckerman and Pease, there were a few very early numerical studies that investigated the thermal performance of MCHS and flow behavior through rectangular ducts [16], [17], [20], [21], [52], [53], [54], [55]. All of these early papers aimed to predict the heat transfer performance or visualize the flow behavior through a numerical analysis or computational fluid dynamics (CFD) simulations.

Knight et al. [18], [19] published two papers, the first considered the work of Tuckerman and Pease and aimed to optimize the channel geometry considering both laminar and turbulent

flow. The second study presented the governing equations for conduction and convection of a heat sink and the fluid dynamics. This was given in the dimensionless form for both laminar and turbulent flow. These equations were applied to the geometries discussed in the previous paper to study the nature of flow (laminar vs. turbulent flow), ratio of fin thickness to channel width and the aspect ratio of the fluid channel. The finding suggested that at low pressure drops, laminar flow dominated which resulted in a lower thermal resistance. Conversely, at higher pressure drops, the optimal thermal resistance was achieved in the turbulent regime. The paper then found an optimized geometry that improved the thermal resistance by 10-35%.

The numerical studies continued into the 2000s and to present day where researchers continued to search for different and unique enhancement strategies for heat transfer in microchannels [15], [56]. Other studies focused on further validating previous works. Fedorov et al. [57] performed a study on a three-dimensional mathematical model of a rectangular channel using incompressible laminar Navier-Stokes equations of motion. The study used a unit cell model which was successful in predicting the flow and heat transfer in the microchannels. The model was validated through comparison of previous experimental papers. The theoretical analysis provided a fundamental understanding of the conjugate conduction-convection heat transfer in the MCHS, distribution of the heat flux and of the flow distribution and boundary layers. The compact heat sink can dissipate a significant thermal load (heat fluxes of the order 100 W/cm^2) with a small increase in the package temperature (less than 20°C), if operated at Reynolds numbers above 150. This theoretical analysis and compared experimental data strongly indicate that the forced convection water cooled microchannel heat sink has a superior potential for application in thermal management of electronic packages.

W. Qu et al. [43] performed a numerical study that used the finite difference method and the SIMPLE algorithm to solve the governing equations. This code was validated using previous analytical and experimental results. The study found that the temperature increase, in the solid fins and in the fluid, in the flow direction, is approximately linear. They also found that fully developed flow may not be reached in the microchannel heat sink at a Reynolds number of 1400 and that by increasing the thermal conductivity of the solid substrate, the temperature at the heated base surface of the heat sink, decreased, in particular, near the channel outlet.

Kandlikar et al. [58] investigated the technological options and challenges of single-phase liquid flow cooling in microchannels. The paper mapped out some of the research opportunities available to meet the future cooling demands for high heat flux IC chips. The study presents several techniques that prove to be promising solutions to further enhance heat transfer in microchannels. This includes increasing the surface area of the fins used in a study, increasing local heat transfer coefficients by periodically introducing flow constrictions to break the boundary layer, incorporating ridges and grooves at specific angles with the flow direction, and introducing mixing features to enhance the mixing between the bulk of the fluid flow and the flow near the channel walls. Dewan et al. [59] further confirmed the benefits presented by Kandlikar et. al and discussed the fundamental mechanisms and validation of continuum theory for incompressible flow in microchannels. The study analyzed parameters such as pressure drop and changes in heat transfer coefficients due to flow conditions and surface roughness. They concluded that flow disruption techniques are effective in enhancing the heat transfer while minimizing the pressure drop consequences. When comparing experimental and numerical studies, if the channel surface characteristics are large enough to impact flow dynamics, they should be included in the models to better predict performance.

2.5. Two-Phase Boiling and Other Cooling Methods

It must be noted that two-phase boiling for cooling high heat fluxes has also proved to be a very promising approach [4], [60], [61]. There are several advantages over single-phase liquid cooling such as, higher heat transfer coefficients, lower flow rates and lower pressure drops for the similar performance [4], [31], [60], [61]. Many studies have performed extensive research on two-phase boiling for cooling applications and most agree that flow boiling is the most promising cooling technology but that it poses many challenges such as flow instabilities. The heat transfer mechanisms are not fully understood and further research is warranted before it can become a viable commercial solution [31]. Consequently, at this time, single-phase cooling offers a more practical solution for high heat flux dissipation.

D. Lee et al. [21] compared the performance of MCHS to jet impingement cooling, another very promising cooling technology. The paper concluded that microchannel cooling is the preferred method for a target dimension smaller than 0.07 m x 0.07 m such as laser diodes or power switching devices and jet impingement is comparable or better for larger targets such as computer chips like central or graphical processing units. D. Lee et al. noted that when manufacturing and maintenance costs are considered, the preferred cooling method still might not be the more suitable choice. In the case of jet impingement, there are still some major complications that need to be addressed such as, potential flow instabilities, high pressure drop, erosion and design complexity [11], [31].

2.6. Research Needs for Microchannel Cooling

The above literature review provides a summary of the current state of research on MCHS. As seen in Table 2-1, a large portion of previous work was performed using heat sinks made of silicon or SiC and water as the cooling liquid. Silicon is a common choice of substrate material

due to its high thermal conductivity. Despite the superior thermal conductivity, previous research has included a variety of heat sink materials and cooling fluids as seen in Table 2-2. Researchers have explored many combinations of heat sink materials and cooling fluids in search of a compatible combination with an improved thermal performance compared to traditional heat sinks. Thermal expansion compatibility is an important consideration for material compatibility when working with high heat flux electronics such as laser diodes. CuW has not been a common substrate material in previous research studies but the coefficient of thermal expansion (CTE) of CuW (CTE of ~ 6.5 x 10^{-6} /K) is closely matched to materials that are commonly used in laser diodes, such as gallium nitride (GaN) (CTE of 5.59 x 10^{-6} /K) and gallium arsenide (GaAs) (CTE of 5.8-6.9 x 10^{-6} /K). Silicon has a CTE of 2.6 x 10^{-6} /K and has comparable thermal conductivity properties to CuW which makes CuW a preferred material for MCHS for laser diode applications. Water is a popular choice for coolant due to its high heat capacity, high thermal conductivity, and low viscosity but it can be corrosive which can lead to stripping ions and charge build up. Additionally, deionized water does not have sufficient voltage hold off in the tested system [38]. This requires additional insulation resulting in increased thermal resistance. FC3283 is a dielectric fluid which may be a potential coolant for microchannel cooling of laser diode arrays. Despite having a significantly lower thermal conductivity than water, FC3283 has a relatively low dielectric constant which makes it compatible with cooling power electronics and a similar viscosity as water. The material properties of silicon, water, and other relevant materials are shown in Table 2-3.

Table 2-3- Thermal Conductivities of Different Materials

Material	Thermal Conductivity
Silicon	k = 130-160 W/m-K
Silicon Carbide	k = 300-400 W/m-K
Copper Tungsten (10/90)	k ~ 180 W/m-K
FC3283	k = 0.066 W/m-K @ 25°C
Water	k = 0.6 W/m-K @ 25°C

Previous research has primarily focused on heat dissipation of a singular, uniform heat sources. Unless the study was used for a specific application, like laser diode cooling, the studies used a single heater bar as the heat source because the primary focus of the research was the heat sink performance. This leaves a gap when considering how a cooling method could benefit discrete heat fluxes like those created from a laser diode bar or laser diode array. Larger, uniform heat sources experience a far lower heat flux than several smaller heat sources. Multiple discretized heat sources, like those created from a laser diode bar, results in a very different heat distribution than a uniform heat source which needs to be considered when designing a MCHS.

2.7. Specific Aims of this Study

This literature review reveals a need for further investigation of new, thermal expansion-matched materials of MCHS and dielectric refrigerants. This work presents the numerical and experimental characterization of single-phase cooling utilizing FC3283 in CuW MCHS for dissipating both discrete and uniform heat fluxes up to 600 W/cm^2. This study will investigate the unique combination of CuW and FC3283 for cooling a uniform, broad area heater and two different discrete heater designs representative of typical laser diode bar profiles. This study outlines a practical approach for microchannels embedded between laser diode bars within an array.

CHAPTER 3. Testing Method

3.1. Test Sections

Three different heater designs were manufactured for this experiment: a broad area heater, a 12-discrete emitter heater, and a 24-discrete emitter heater. Each of these heaters consists of a thin film, platinum heater bonded to a CuW heat sink. All heaters have a footprint of 2.5 mm × 10 mm (L × W) and are located 1mm downstream from the channel inlet. Two gold coated electrical contact pads are located on the sides of the heater for pogo pin connections. In-between the heater and CuW cold plate was a 76.2 AlN spacer to provide electrical isolation from the metallic cold plate. Conductive epoxy was applied between the contact pad and the heat sink to ground the test section and prevent shorting from electrostatic charge built up in the fluid due to contact with plastic tubing.

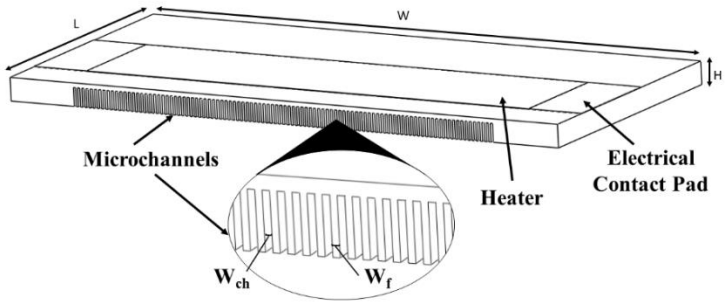

Figure 3-1- Schematic of test sections.

3.1.1. Microchannels

The heat sinks were fabricated using a dicing saw to create channels and fins that are roughly 100 µm wide and 365 µm deep. The resulting hydraulic diameter of the channels is approximately 160 µm. Figure 3-1 shows a schematic and Figure 3-2 displays an image of the CuW microchannels. Designing a heat sink with deeper channels improves the overall cooling

performance by increasing the amount of surface area to enhance the heat transfer with the fluid. Since this work contains a unique material combination that has not been used before, this study is the initial proof-of-concept experiment. Because of this, the MCHS were created prior to conducting a microchannel optimization study. 100 µm wide channels are much simpler to fabricate compared to smaller channels and they allow for symmetry to be utilized in the discrete emitter CFD model creation due to the matching width of a fin and channel to one emitter. There will always be tradeoffs in pressure drop and performance, using a larger channel geometry allows for increased flow rates to attempt to increase performance with increased developing length and flow regime transition. Electrically conductive epoxy was applied between the heat sink and the low voltage side contact pad, serving as a ground to the test section. This grounding action helped prevent the test section from short circuiting due to electrostatic charge accumulation in the dielectric fluid due to friction with the plastic tubing. A Keyence KK-X200 was used to measure the widths of the fin and channels as seen in Figure 3-3. Table 3-1 shows the test section geometries and the respective measurement uncertainties.

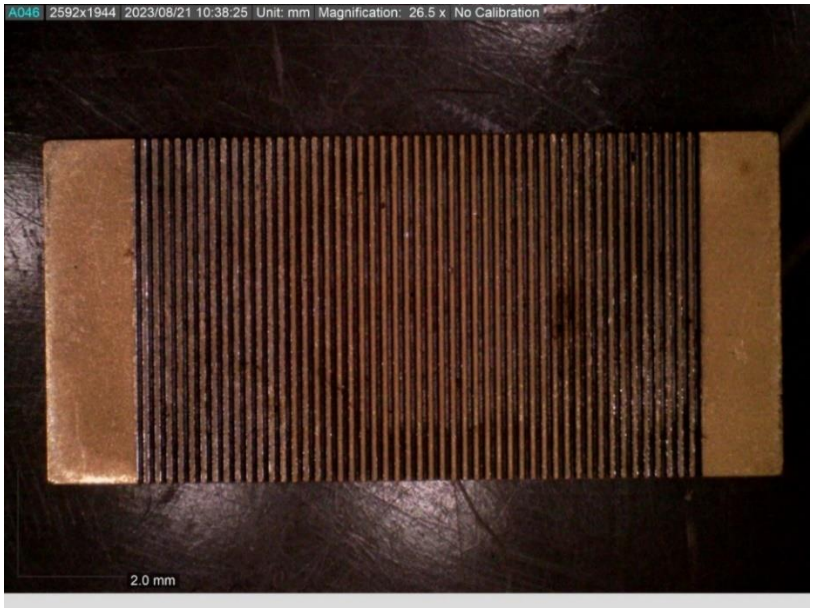

Figure 3-2- Image of microchannels.

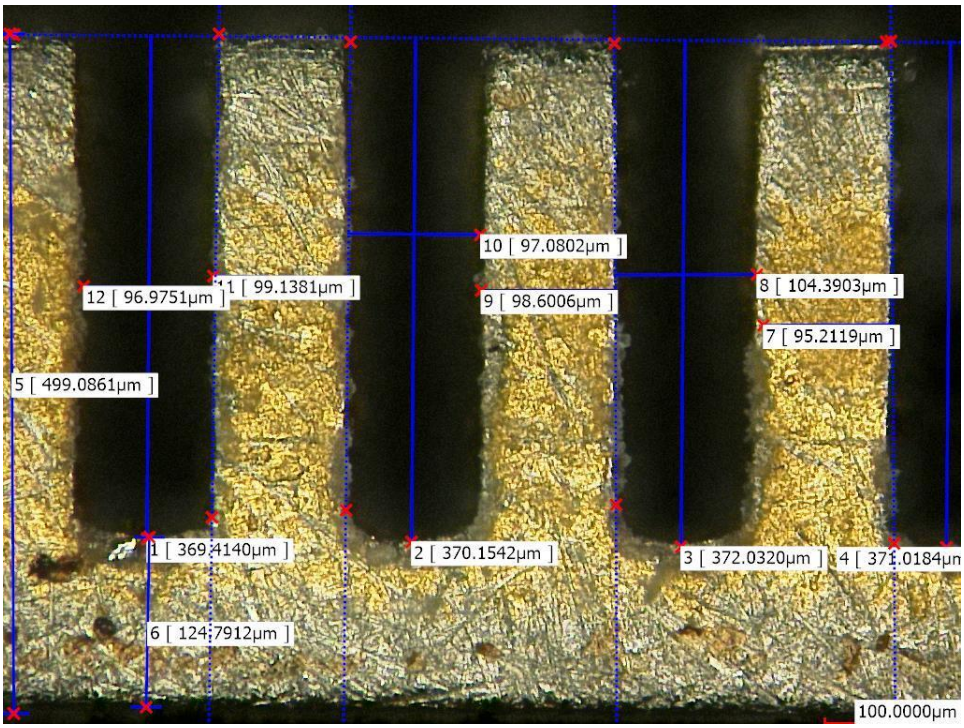

Figure 3-3- Measurement image of microchannels.

Table 3-1- Test Section Geometry

Measurement	Broad Area	24 Emitter	12 Emitter	Uncertainty
Channel Length	6.2 mm	6.2 mm	6.2 mm	+/- 5µm
Base Thickness	129 µm	119 µm	128 µm	+/- 5µm
Average Channel Width (W_{ch})	101 µm	114 µm	97 µm	+/- 3µm
Average Fin Width (W_f)	96 µm	87 µm	98 µm	+/- 5µm
Average Channel Depth	364 µm	369 µm	365 µm	+/- 5µm

3.1.2. Broad Area

The broad area test section consists of a platinum heater spanning the entire length of the footprint where the heat load is evenly distributed across the entire heater. Figure 3-4 shows the schematics of the broad area heater and Figure 3-5 displays an image of the fabricated broad area heater.

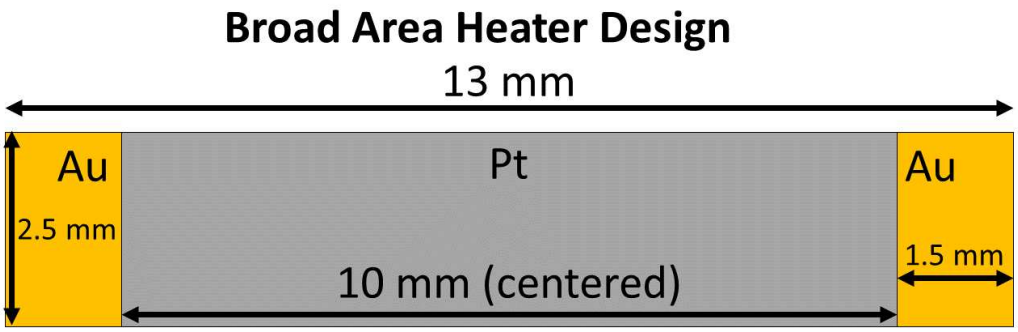

Figure 3-4- Schematic of broad area heater design.

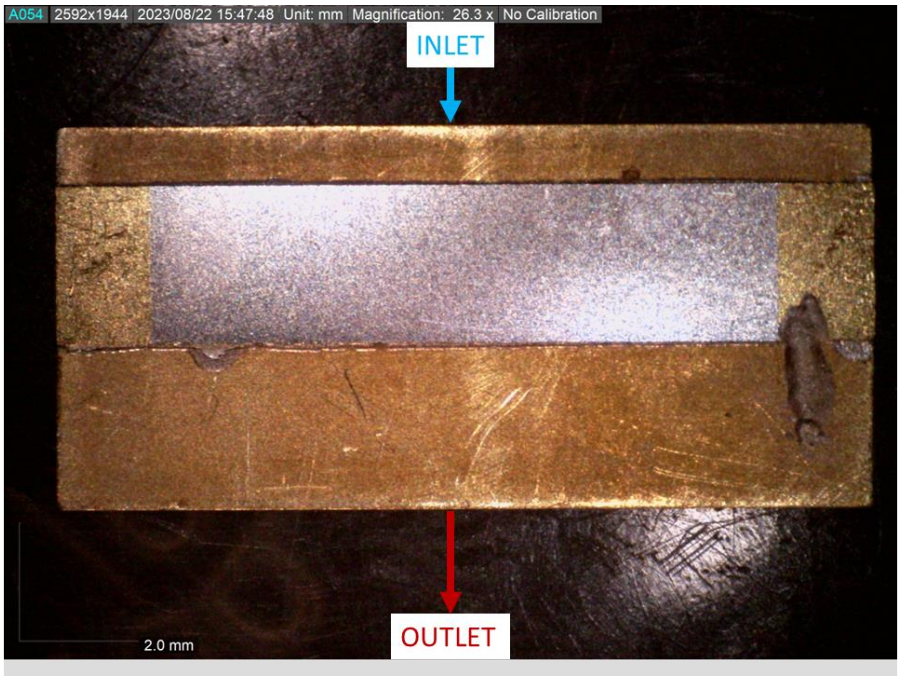

Figure 3-5- Image of broad area test section.

3.1.3. Discrete Emitters

The discrete emitter test sections were designed similarly to the broad area heater but contain an additional gold layer which divides the platinum heater into 12 or 24 separate exposed areas of the heater. These separate exposed areas act as surrogate discrete laser diode emitters. In both test sections, the emitters are 200 µm wide but have a different pitch between the emitters. The 12-emitter test section has an 800 µm pitch and the 24-emitter test section has a 400 µm pitch between emitters. Figure 3-6 and Figure 3-8 show the schematics of the 12-emiter and 24-emitter

heaters respectively. Figure 3-7 and Figure 3-9 display images of the fabricated 12-emiter and 24-emitter heaters respectively.

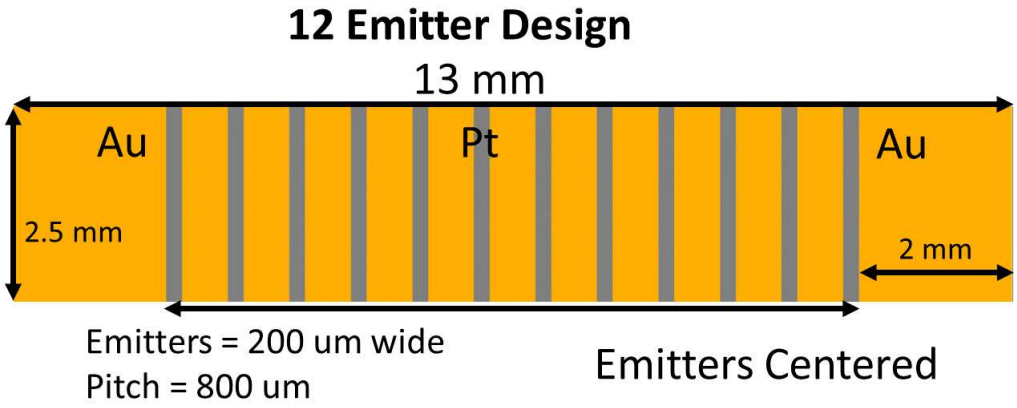

Figure 3-6- Schematic of 12-emitter heater design.

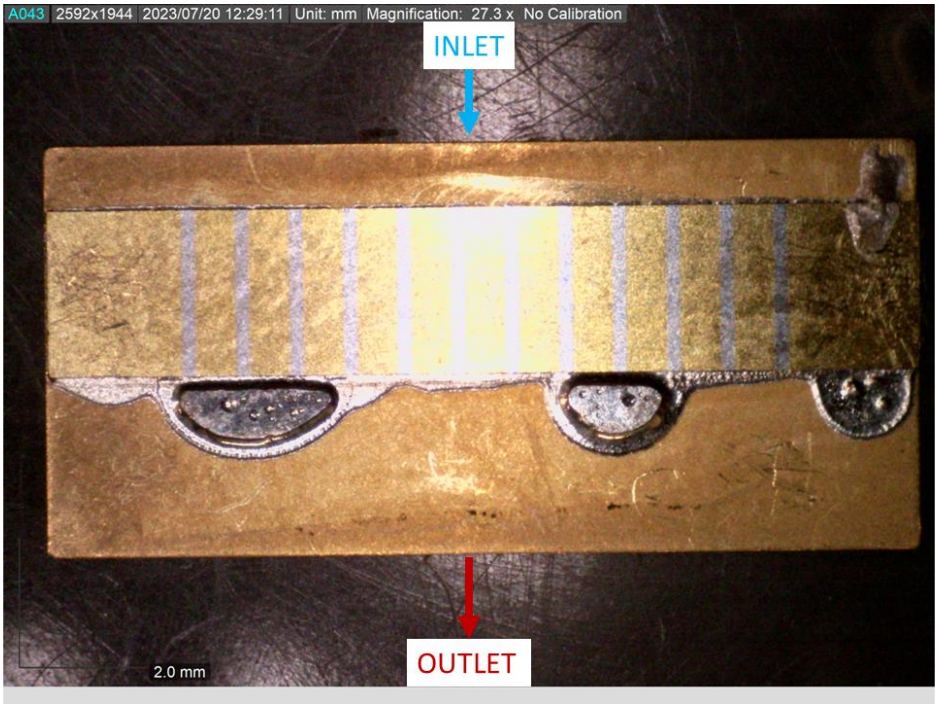

Figure 3-7- Image of 12-emitter test section.

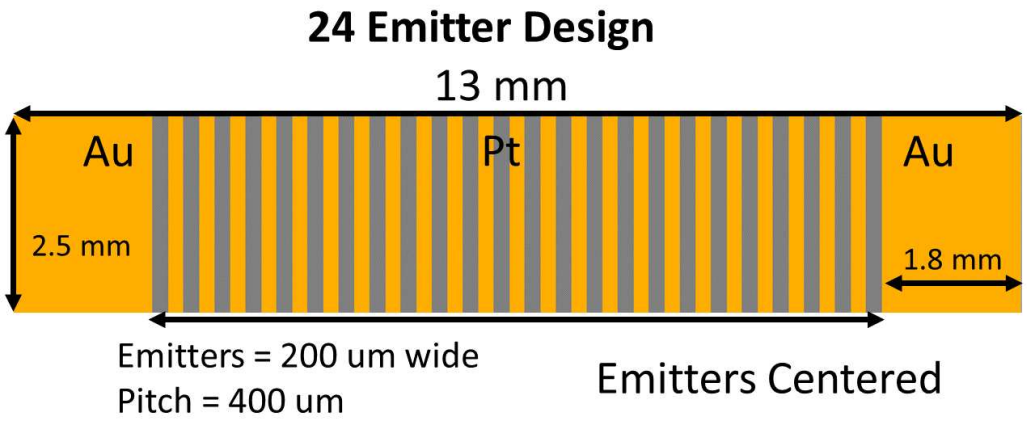

Figure 3-8- Schematic of 24-emitter heater design.

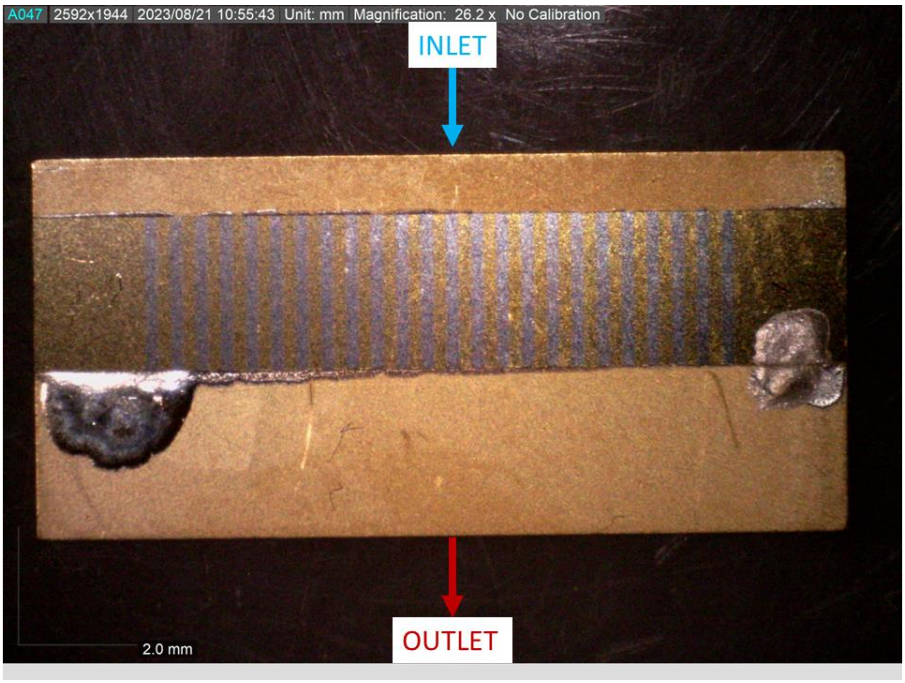

Figure 3-9- Image of 24-emitter test section.

3.2. Manifold Design

The manifold used to place the test section within the cooling facility was fabricated with PEEK. Thermocouple and pressure ports were drilled into the top PEEK plate and an O-ring was placed between the top and bottom PEEK plates to seal the fluid within the manifold. A fluorosilicone

gasket was machined to seal around the heater to prevent any fluid leakage from the IR viewing window. Within the manifold were two T-type thermocouples (Omega SCPSS-062G-6) and two pressure transducers (Omega PX319-100GI and Dwyer 7808493 0-100 psi) at the inlet and outlet ports to observe the changes across the microchannels. The location of the thermocouples and pressure sensors can be found in Figure 3-10. The thermocouples and pressure transducers were calibrated prior to testing. The uncertainty for all the instruments used in the test facility can be found in Table 3-4 and further details can be found in the uncertainty section at the end of this chapter. High conductivity pogo pins with high spring force (QA Tech 100-25 Series) were used as the electrical connections to the test section within the manifold. A schematic and an image of the fluidic manifold is shown in Figure 3-11 and Figure 3-12 respectively.

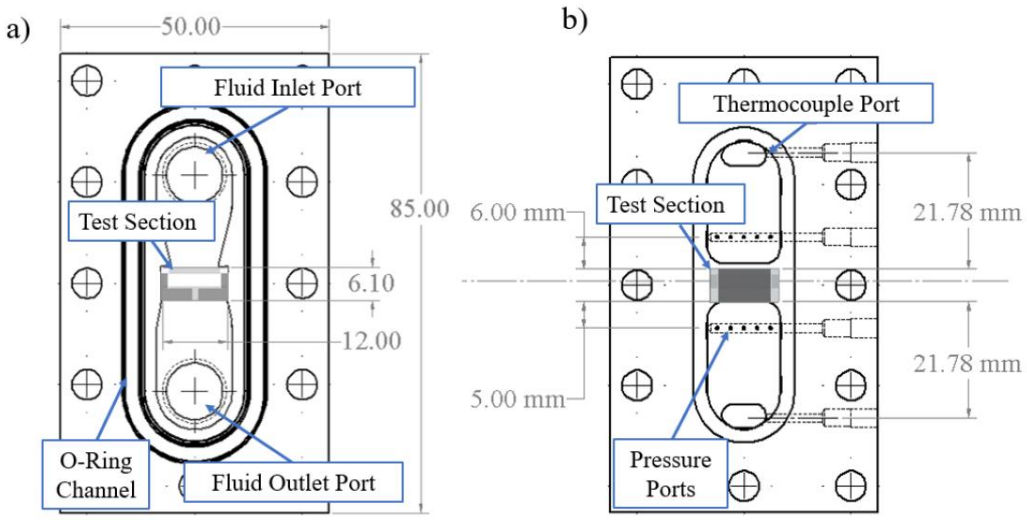

Figure 3-10- Internal schematic of manifold. Bottom view drawing of the manifold PEEK top plate with test section in place. The thermocouple ports upstream and downstream are located 21.78 mm from the inlet and outlet of the channels. The upstream pressure port is 6 mm from the channel inlet, while the downstream pressure port is 5 mm from the channel exit. The fluid travels through a 1.5 mm gap from the inlet port to the channels.

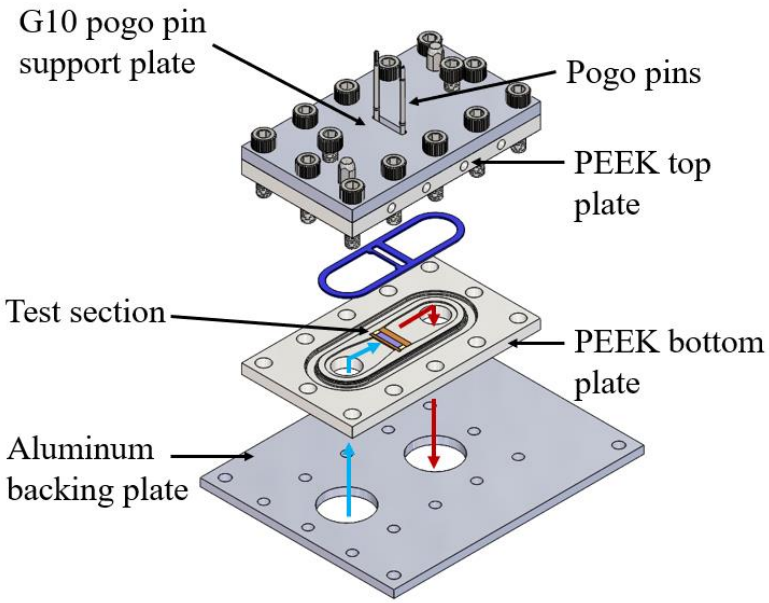

Figure 3-11- Exploded view of manifold.

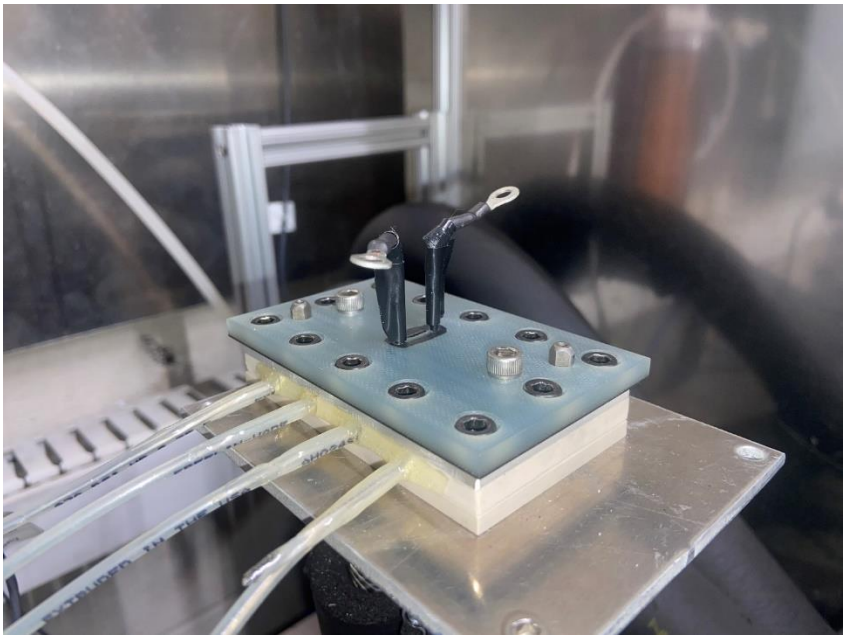

Figure 3-12- Image of manifold.

3.3. Experimental Set Up

3.3.1. Facility Design

A schematic of the test facility is shown in Figure 3-13. The cooling fluid, FC3283, entered the manifold inlet at approximately 10°C. The fluid was pulled from a reservoir and circulated through

the loop using a gear pump (Micropump GC-M25). The FC3283 was cooled using two heat exchangers (Kelvion GBS-200H-16) which are provided with chilled water from a Polystat Cole-Parmer chiller. The cooled fluid was then passed through a Coriolis flow meter (Rheonik RHM 04) to measure and control the flow rate. Flow then entered the manifold at the desired flow rate and after passing through the test section, exited at a higher temperature and reentered the heat exchangers to be cooled and then recirculated through the facility. Rubber foam insulation was wrapped on the outer surfaces of the tubing to minimize the heat loss to the environment.

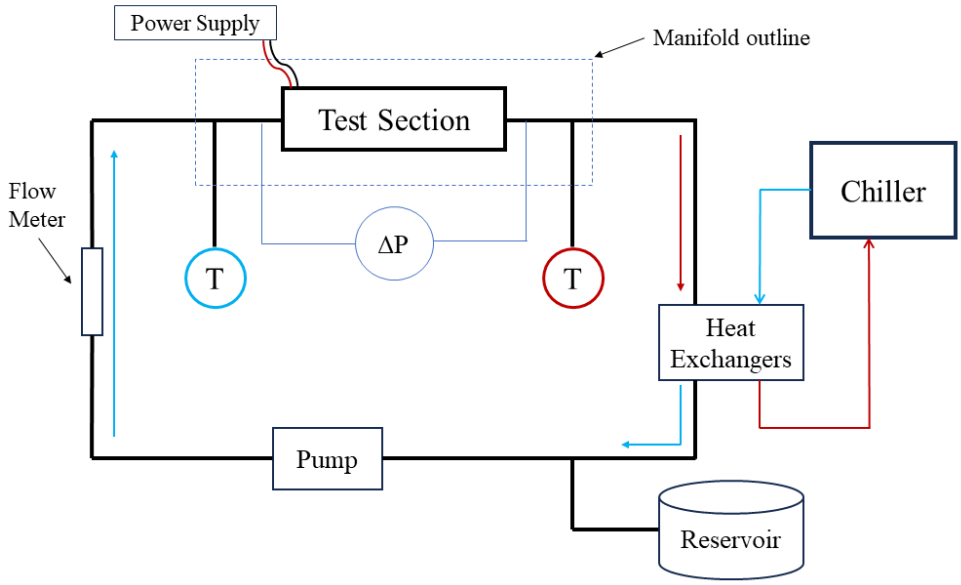

Figure 3-13- Schematic of test facility.

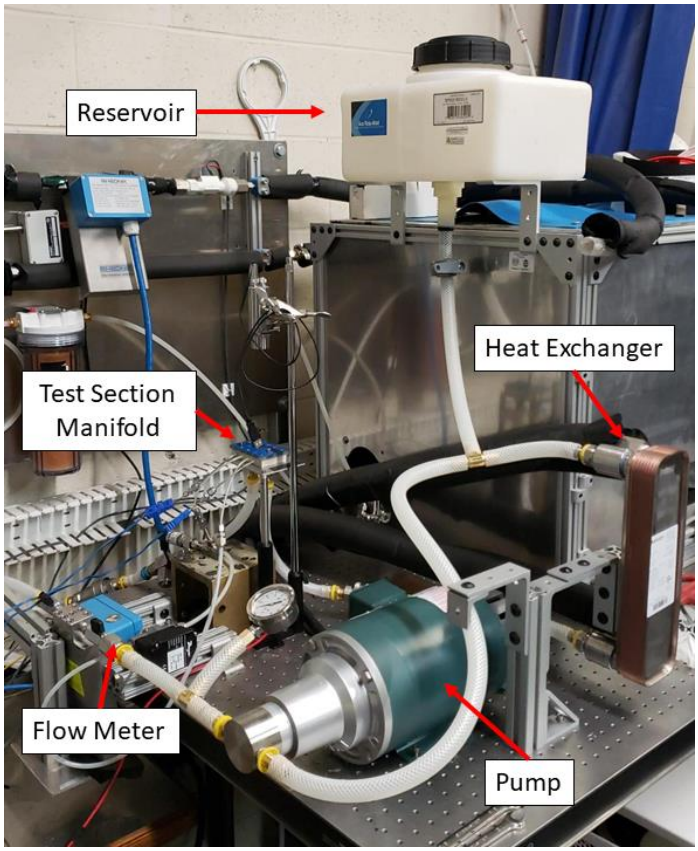

Figure 3-14- Image of test facility.

3.3.2. Test Parameters

The experiment consisted of applying incremental power loads to the test section at various flow rates. When the system reached a steady state with an inlet temperature of 10°C, power was applied to the heater using an HP 6030A system power supply. The power was increased by 25 W until reaching a max of 150 W. Once a steady state was reached at each power load, data was recorded before incrementing to the next power load. This test was repeated at several different flow rates ranging from 0.5 kg/min to 2 kg/min. Table 3-2 lists the flow rates tested.

Table 3-2- Tested Flow Rates

Test Section	Tested Flow Rates (kg/min)						
Broad Area	0.5	0.75	1.0	1.25	1.5	1.75	2.0
12-Emitter	0.5	-	1.0	-	1.5	-	2.0
24-Emitter	0.5	-	1.0	-	1.5	-	2.0

3.3.3. Data Acquisition

A National Instruments data acquisition module (cDAQ 9174) was used to observe data, such as voltage, current, resistance, inlet and outlet temperature, and pressure drop, from the measurement devices. Voltage and current were measured between the leads of the high conductivity pogo pins. An Agilent 34401A digital multimeter was used to measure voltage and a Keysight 34465A digital multimeter was used to measure current. This data was then monitored and recorded in a custom LabVIEW program at 1 Hz.

3.3.4. Temperature Measurement

The average heater temperature was determined by converting the measured electrical resistance to temperature based on an independent calibration of the test sections performed by measuring the electrical resistance as a function of temperature. Each test section was placed in the environmental chamber alongside a high accuracy thermometer (+/- 0.012 °C reference thermometer) and the temperature ranged from 18°C to 95°C while the resistance across the test section was measured and recorded. The maximum electrical resistance uncertainty was <0.01 Ohm and did not appreciably change the curve fit uncertainty upon its inclusion; it was therefore neglected. A curve fit was then applied against the temperature and resistance resulting in the following equations found in Table 3-3.

Table 3-3- Temperature Equations from Electrical Resistance Calibration

Test Section	Temperature Equation	Temperature Uncertainty
Broad Area	$T = 72.85R - 424.7$	+/- 0.6°C.
12-Emitter	$T = 57.75R - 471$	+/- 0.6°C.
24-Emitter	$T = 31.51R - 492.7$	+/- 0.5°C.

where T is the average heater temperature and R is the measured resistance from the experimental test.

3.3.5. Measurement and Instrument Uncertainty

The uncertainty values for the calculated and measured experimental values were calculated using the root sum square method. In this method, the total uncertainty for any variable X is calculated according to Equation (4).

$$\delta X = \sqrt{BE^2 + PE^2} \tag{4}$$

Where BE is the bias error and PE is the precision error. The precision error was determined by calculating the 95% confidence interval from the standard error and two-tailed t-value for each average value of the inlet fluid temperature, pressure drop, voltage and current. The bias error was determined from the datasheet provided for each measurement instrument or was propagated accordingly for each calculated variable.

The thermocouples and pressure transducers were calibrated prior to experimental testing. The thermocouples were calibrated using a high accuracy reference thermometer (+/- 0.012 °C) in a thermal bath ranging from 0°C to 95°C and the pressure transducers were calibrated against a deadweight tester with +/-0.1 psi uncertainty. The thermal resistance is calculated using ΔT and Q; therefore, to calculate the uncertainty in thermal resistance, a weighted least squares linear regression and effective variance method was used. An iterative method must be used to solve for the thermal resistance which requires an initial guess of thermal resistance ($R_{th,guess}$) using an unweighted least squares regression. A minimization target in terms of thermal resistance is shown in Equation (5) where the value of $S_{EV,2}$ is minimized through iteration by changing the value of $R_{th,guess}$.

$$S_{EV,2} = \sum \frac{(\Delta T_i - R_{th,guess} q_i'')^2}{\delta \Delta T_i^2 + (R_{th,guess} \delta q_i'')^2} = \sum \frac{(\Delta T_i - R_{th,guess} q_i'')^2}{e_i^2} \tag{5}$$

This iteration process is repeated until the value of the initial guess is equal to the calculated thermal resistance with the weighted variance. e_i^2 is the weighted variance calculated for each data point. The slope error is then calculated using Equation (6).

$$U_{R_{th}} = \frac{\sqrt{\frac{\sum(\Delta T_i - R_{th} q_i'')^2}{N_S - 1}}}{\sqrt{\sum \frac{q_i''^2}{e_i^2}}} \tag{6}$$

The uncertainty was then multiplied by a t-value calculated from a 95% confidence interval. Table 3-4 lists the uncertainty for all the instruments used in the test facility.

Table 3-4- Uncertainty of Measurement Instruments

Instrument	Total Uncertainty
Thermocouples	+/- 0.3°C
Pressure Transducers	+/- 2 kPa
Mass Flow Meter	+/- 0.004 kg/min
Heat Load	+/- 0.1 %
Heater Resistance	+/- <0.01 Ohm
Average Heater Temperature	+/- 0.5°C - 0.6°C
Thermal Resistance	+/- 0.001 cm^2K/W

CHAPTER 4. Modeling Approach

A model was created using the COMSOL Multiphysics software which is a simulation platform used for building and solving CFD models. COMSOL is a finite element solver method which can be useful when looking at problems that contain coupled phenomena such as heat transfer and fluid dynamics. This chapter will discuss the modeling approach for building and solving this simulation which was used to validate the experimental results.

4.1. Computational Domain

A numerical model was created in COMSOL MultiPhysics v6.1 to compare and validate the experimental results. A validated computational model can be helpful for providing predictions for future work. A full heat sink in this study has 50 channels which would make a large and complex CFD model with lengthy computational time. By utilizing the symmetry within a heat sink, a smaller unit cell model was created for each test section that captured the physics of the heat transfer within either one or two channels, as explained below. Figure 4-1 displays the selection and symmetry used to extract a unit cell model from the entire test section and Figure 4-2 shows the unit cell model geometry that was built within COMSOL. The results from these smaller models can then be mirrored to represent a full model. The broad area unit cell model consisted of one-half channel and a half fin. The discrete emitter unit cell models are slightly different to include an emitter and the spacing between the emitters. The 12-emitter model consisted of half an emitter, half the spacing distance between the emitters, and two channels with a fin in between and half fins on each end. Similarly, the 24-emitter unit cell model had half an emitter and half the spacing distance between the emitters but had only one channel with a fin in between and half fins on each end. Additionally, each unit cell model included an inlet plenum

region to account for the large pressure drop that occurs as the fluid is forced into the microchannels.

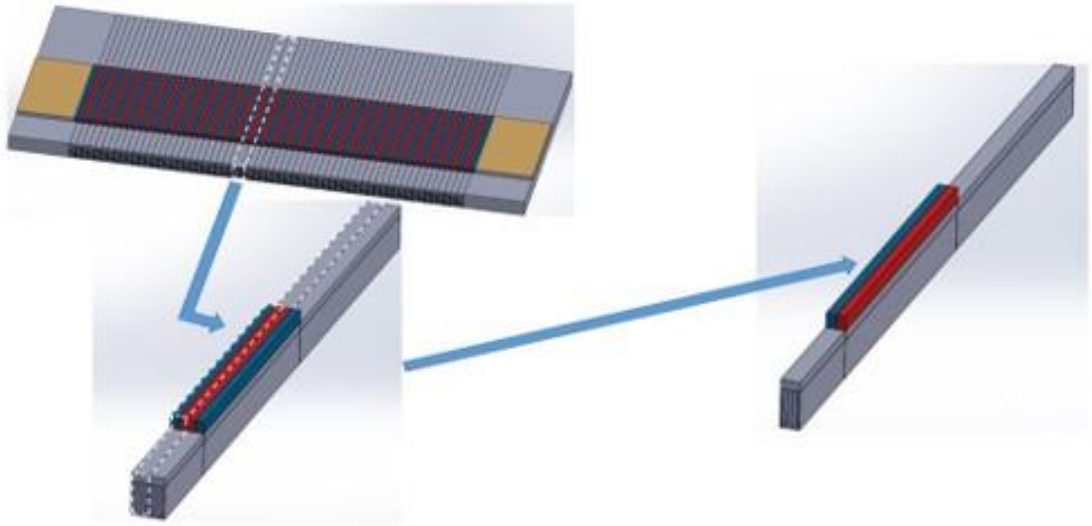

Figure 4-1- Unit cell model selection.

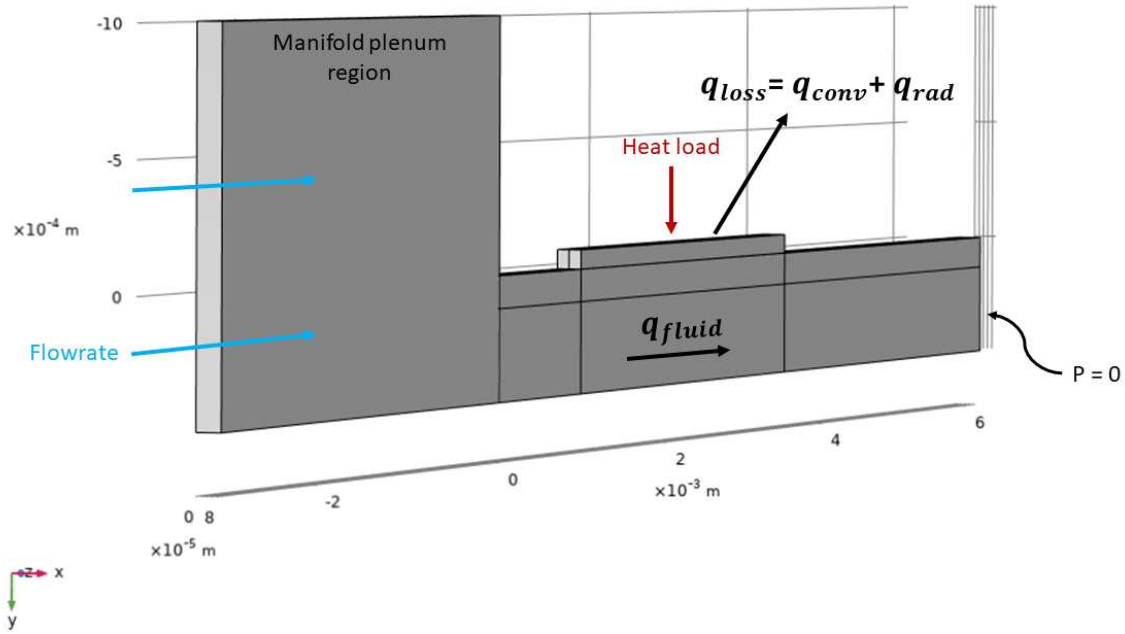

Figure 4-2- Unit cell model geometry.

4.2. Governing Equations and Boundary Conditions

The model was built using a coupled 3D heat transfer formulation which combines heat transfer with computational fluid dynamics in COMSOL MultiPhysics v6.1. All models assumed steady, incompressible, laminar flow due to the low Reynolds numbers, between 0-1500, and the steady operating conditions. COMSOL contains built-in physics, and this model was created using COMSOL's *Nonisothermal Flow* coupling interfaces which includes the heat transfer in solids and fluids physics and the laminar flow physics. The following governing equations are the fluid and energy equations solved within the COMSOL model.

$$\rho(\nabla \cdot \vec{u}) = \nabla \cdot [-P\vec{I} + \mu\overrightarrow{\nabla u}]. \tag{7}$$

$$\rho c_p \vec{u} \cdot \overrightarrow{\nabla T} = \nabla \cdot \left(\mathrm{k}\overrightarrow{\nabla T}\right) \tag{8}$$

A constant thermal conductivity of 180 W/(m-K) was used for CuW within the model and temperature-dependent fluid properties were used for FC3283 from the manufacturer-provided datasheets. The measured experimental values were used as the inlet temperature values and the inlet mass flow rates in the channels. Experimental values were also used for the applied heat load which was then scaled down to the unit cell dimensions. The channel outlet gauge pressure was set to zero so the inlet pressure calculated would be the pressure drop across the channels.

All external surfaces of the model that were not assuming symmetry, were set as insulated surfaces with the exception of the heater. The entire test section is held in a PEEK manifold which has a low thermal conductivity (~0.25 W/(m-K)), minimizing heat loss around the test section. There is a viewing window cut into the PEEK top plate which can be seen in Figure 3-11. This viewing window exposes the heater to the environment and causes additional convective and radiation losses. Radiation and natural convection boundary conditions were set on the heater surface to account for any heat loss to ambient. The model assumed an emissivity of 1 and ambient temperature was set to 70°F (21.1°C).

The heat loss in the model is calculated according to Newton's Law of Cooling (9) and the convective and radiative heat transfer coefficients are calculated according to Equation (10) and Equation (12) respectively.

$$Q_{loss} = (h_{conv} + h_{rad})A_h(T_h - T_{amb}) \quad (9)$$

$$h_{conv} = 0.54Ra_{L_C}^{1/4}\frac{k_{air}}{L_C} \quad (10)$$

$$Ra_{L_C} = \frac{g\beta(T_h + T_{amb})L_C^3}{v\alpha} \quad (11)$$

$$h_{rad} = \epsilon\sigma(T_h^2 + T_{amb}^2)(T_h + T_{amb}) \quad (12)$$

All air properties are evaluated at the film temperature $T_{film} = (T_h + T_{amb})/2$, $L_C = W_h L_h/2(W_h + L_h)$, $\sigma = 5.67 \cdot 10^{-8}$ W/m^2-K^4, and $\epsilon = 1$. The maximum heat loss from the heater to ambient was found to be 0.16 W for the 12-emitter mode, 0.14 W for the 24-emitter model and 0.13 W for the broad area model. The h_{conv} values ranged from 11-24 W/m^2-K for all three test sections and h_{rad} values ranged from 6-13 W/m^2-K for all three test sections.

4.3. Mesh Sensitivity Analysis

A mesh sensitivity study was performed to understand the impact of mesh coarseness on the model results. Mesh refinement analyses are necessary for determining a balance between result accuracy and computational cost. This study was conducted at the highest and lowest flow rates for each test section while using average heater temperature and pressure drop as the observable metrics. The lowest flow rates experience the largest temperature gradients, while the highest flow rates experience the largest inertial and viscous forces. Figure 4-3 displays the results from the mesh sensitivity study for the broad area model. For the broad area test section, the differences in temperature between the coarsest mesh to the medium number of elements was < 0.9% and difference in pressure drop was < 0.8%. The differences in temperature between the

finest mesh to the medium number of elements was < 0.4% and difference in pressure drop was < 0.25%. The two discrete models had similar results to the broad area. Due to the smaller difference between the finest mesh and the medium mesh, the medium mesh size was used to reduce the computational cost while the loss in accuracy remains negligible.

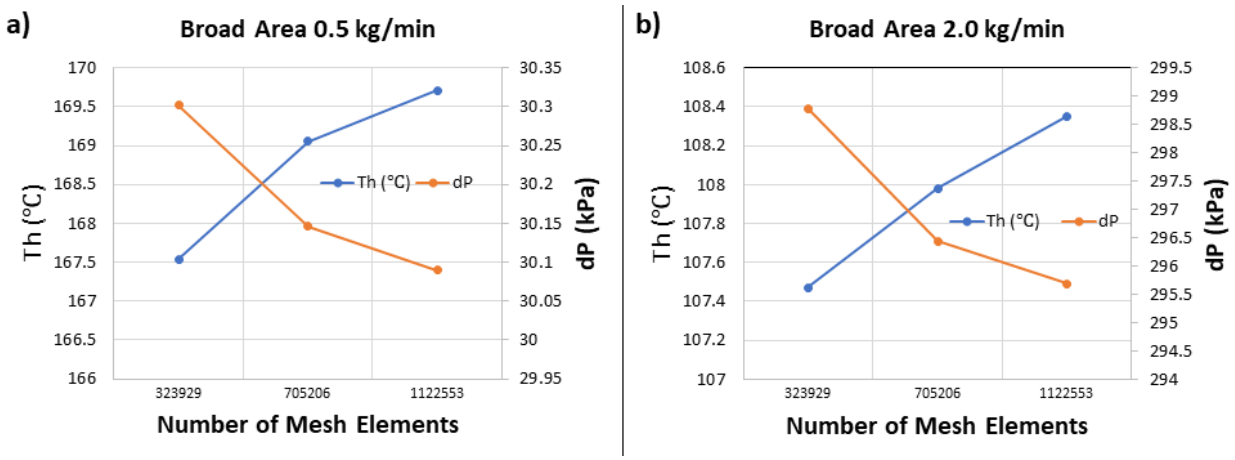

Figure 4-3- a) Mesh sensitivity analysis for the broad area model at 0.5 kg/min with average heater temperature and pressure drop plotted against different number of mesh elements. b) Mesh sensitivity analysis for the broad area model at 2.0 kg/min with average heater temperature and pressure drop plotted against different number of mesh elements.

CHAPTER 5. Results and Discussion

The previous two chapters outlined the experimental methods and the CFD modeling approach. This chapter will present the results obtained from both the experiments and the modeling efforts. First, the experimental results for the broad area heater and the 24-emitter heater will be presented because they have the most similar heater behaviors, similar geometries, and comparable models. The experimental results will also be compared to the model results. Next, the experimental and model results will be presented for the 12-emitter test section. Finally, the chapter will conclude by comparing the temperature distribution and thermal resistances of all three test sections studied.

5.1. Broad Area and 24 Emitter

Figure 5-1 and Figure 5-2 show the average heater temperature for each power load and flow rate tested for the broad area and 24-emitter test sections. The maximum average heater temperature observed on the broad area test section was 159°C at 0.5 kg/min and the maximum average heater temperature observed on the 24-emitter test section was 162°C at 0.5 kg/min. The average heater temperatures for these two test sections are very similar to each other, which is expected. The 24-emitter test section design behaves very similarly to the broad area test sections because the emitters are very close together resulting in significant heat spreading between the emitters. Figure 5-3 compares the experimental average heater temperature to the model's prediction for both the broad area test section and 24-emitter test section. For the broad area test section, at the highest flow rate, all simulation predictions were within 4% of the experimental results and for the 24-emitter test section, at the highest flow rate, all simulation predictions were within 5% of the experimental results.

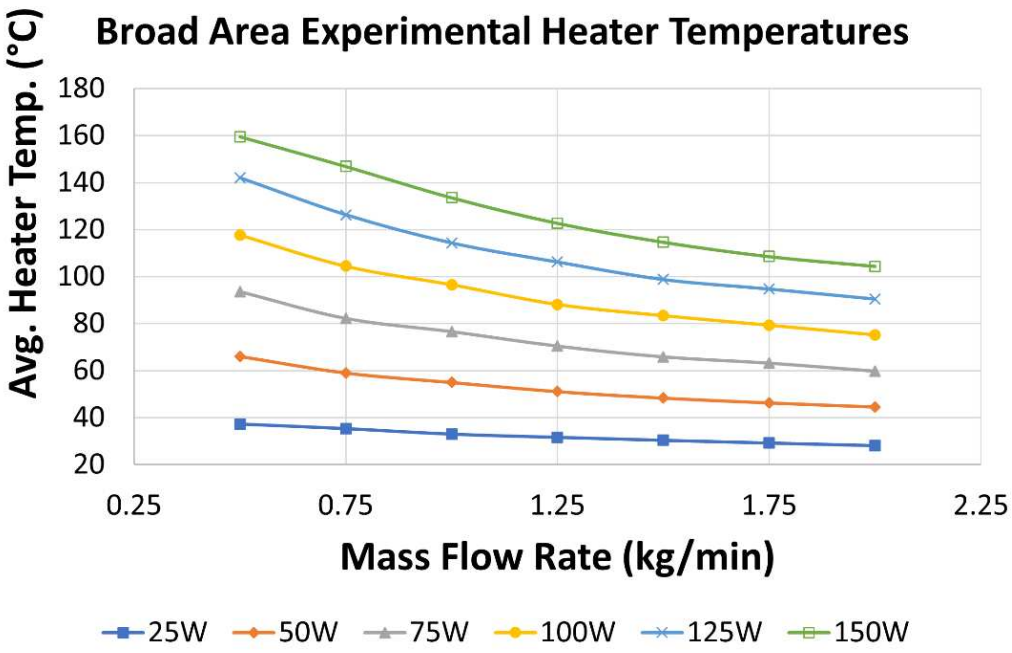

Figure 5-1- Average broad area heater temperature at each power load for each flow rate.

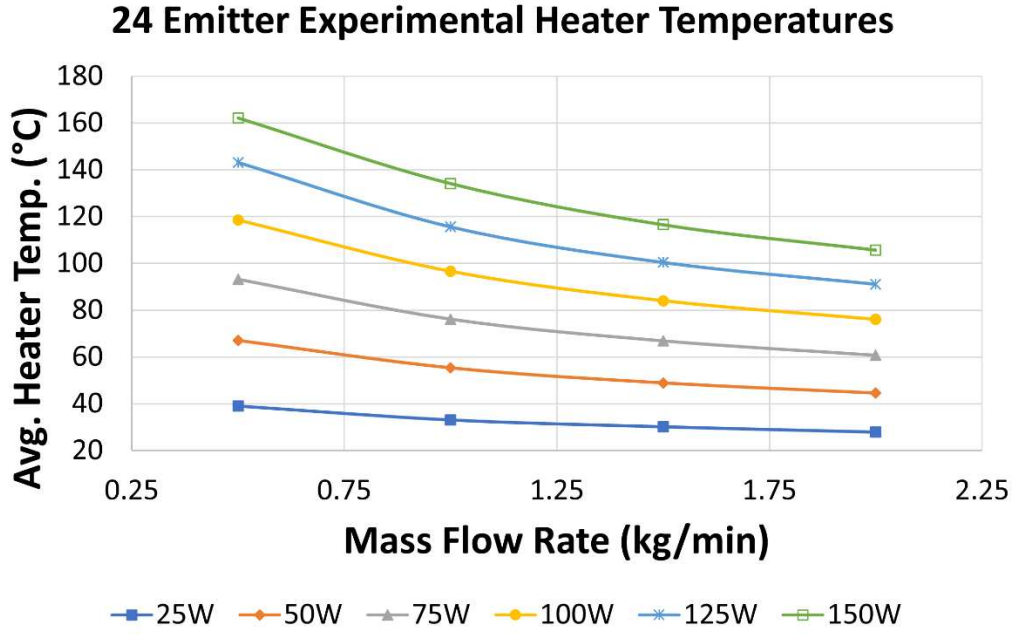

Figure 5-2- Average 24-emitter heater temperature at each power load for each flow rate.

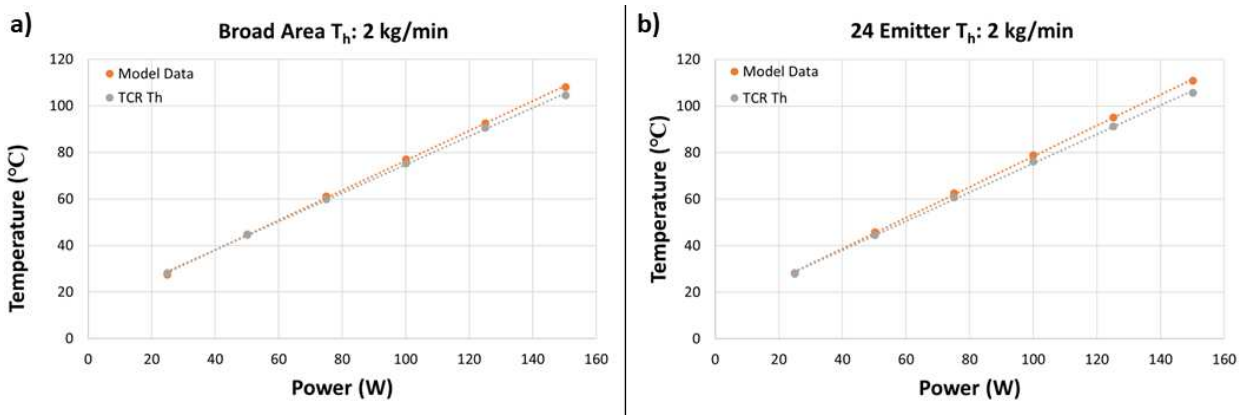

Figure 5-3- a) Experimental and model comparison of average heater temperature vs power load at 2 kg/min for the broad area heater. b) Experimental and model comparison of average heater temperature vs power load at 2 kg/min for the 24-emitter heater

Figure 5-4 displays the average pressure drop for the lowest and highest heat loads tested across the varying Reynolds numbers reached for the broad area and 24 emitter test section. Similarly, Figure 5-5 shows the average pressure drop for the lowest and highest flow rates across the power loads tested. The maximum pressure drop observed experimentally for the broad area test section was approximately 326 kPa at a flow rate of 2 kg/min and was 356 kPa for the 24-emitter test section also at a flow rate of 2 kg/min. The higher pressure drop observed in the 24-emitter test section is due to the smaller channel width which can be seen in Table 3-1. By comparing Figure 5-1 and Figure 5-2 to Figure 5-4 and Figure 5-5, one can see that the cooling performance comes at a tradeoff: the average heater temperatures are lower at the highest flow rates but the consequence is high pressure drops which requires an increase in pumping power.

These graphs also show the predicted pressure drop conditions from the models. Overall, for the broad area and 24-emitter test sections, the predicted pressure drop matched the experimental results, although the model slightly underpredicts the measured pressure drop at higher flow rates. The simulation predictions for the broad area were within 10% of the experimental results and on average were within 15% of the experimental results for the 24-emitter test section.

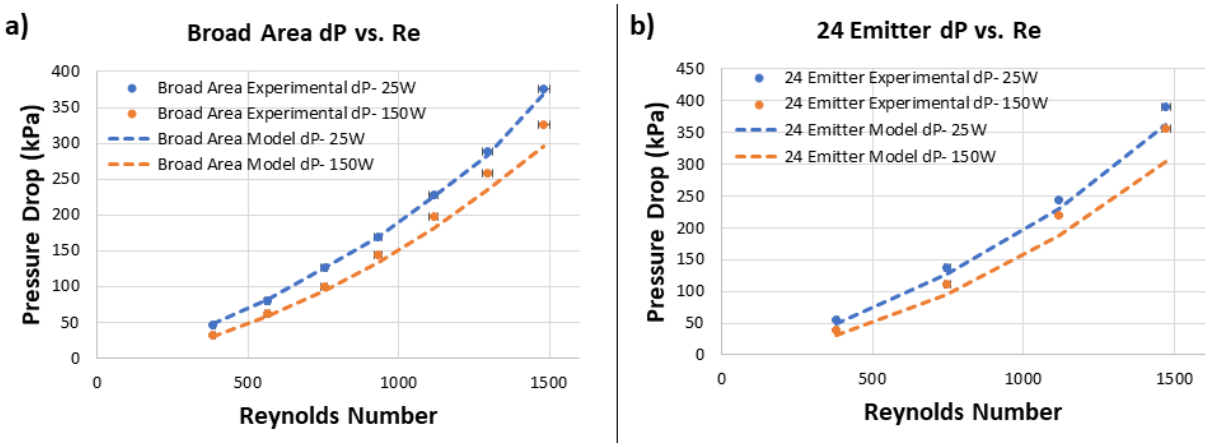

Figure 5-4- a) Broad area test section simulation and experimental comparison of pressure drop across the microchannels across all the tested flow rates, at the lowest and highest heat load. b) 24-emitter test section simulation and experimental comparison of pressure drop across the microchannels across all the tested flow rates, at the lowest and highest heat load.

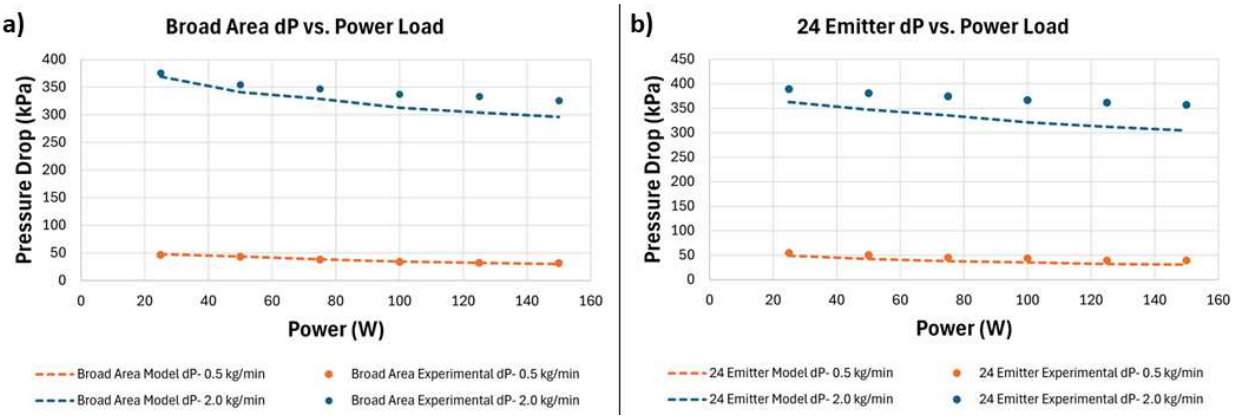

Figure 5-5- a) Broad area test section simulation and experimental comparison of pressure drop across the microchannels across all the power loads tested, at the lowest and highest flow rate. b) 24-emitter test section simulation and experimental comparison of pressure drop across the microchannels across all the power loads tested, at the lowest and highest flow rate.

5.2. 12 Emitter

Figure 5-6 show the average heater temperature for each power load and flow rate tested for the 12-emitter test sections. The maximum average heater temperature observed on the 12-emitter test section was 169°C at 0.5 kg/min. The average heater temperatures for this test section are higher than both the 24-emitter and the broad area test section due to the higher heat flux in each individual

emitter. Figure 5-7 compares the experimental average heater temperature to the model's prediction at the highest flow rate. For the 12-emitter test section, all simulation predictions were within 7.5% of the experimental results.

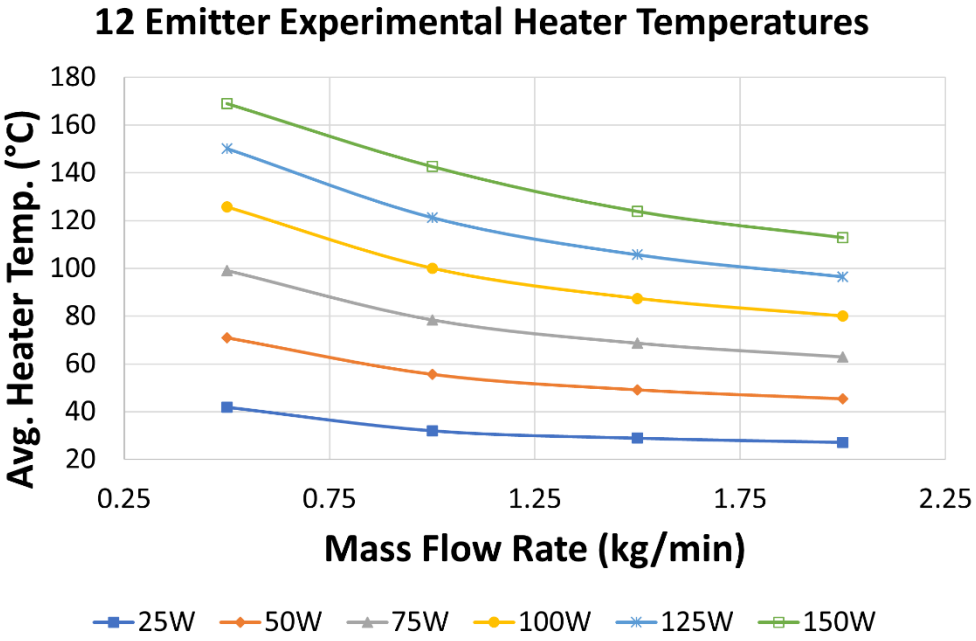

Figure 5-6- Average 12-emitter heater temperature at each power load for each flow rate.

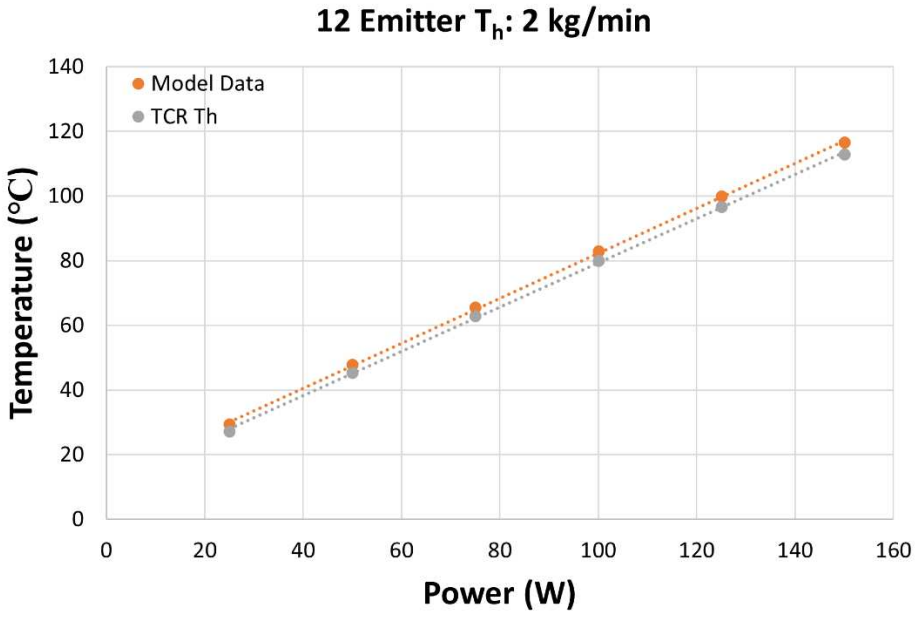

Figure 5-7- Experimental and model comparison of average heater temperature vs power load at 2 kg/min for the 12-emitter heater.

Figure 5-8 shows the modeled and measured average pressure drop versus Reynolds number for the 12-emitter test section at the lowest and highest heat loads tested. Similarly, Figure 5-9 shows the average pressure drop for the lowest and highest flow rates across the power loads tested. The maximum pressure drop observed experimentally for the 12-emitter test section was approximately 309 kPa at the highest flow rate of 2 kg/min and a heat load of 150 W while the maximum pressure drop predicted by the model was significantly lower at 222 kPa at the same test conditions.

One can see that in the 12-emitter figures there is a larger difference in pressure drop between the experimental results and the model predictions than the broad area and 24-emitter figures. There are several possible sources for this discrepancy between the model and test results, especially at higher flow rates. One possible factor is that due to the larger spacing between the emitters; to make a symmetric unit cell model, two channels were required in a single unit cell model. This is a significant difference from the broad area and 24-emitter models which only have one channel. There may be some laminar to turbulent transitional flow behavior occurring in the channels at higher flow rates not captured by the model. If there is some transitional flow occurring in the experiments, we would expect to see higher pressure drops than a model which is using laminar flow which is clearly seen in these figures. There is a larger difference between the model and the experimental results at the higher flow rates for all three test sections but due to the 12-emitter unit cell model having two channels instead of one, this could be causing a larger difference between experimental results and the simulation predictions for the 12-emitter test section. Overall, this 12-emitter model reasonably captures the physics by projecting the correct trend, but it underpredicts the pressure drop especially at higher flow rates.

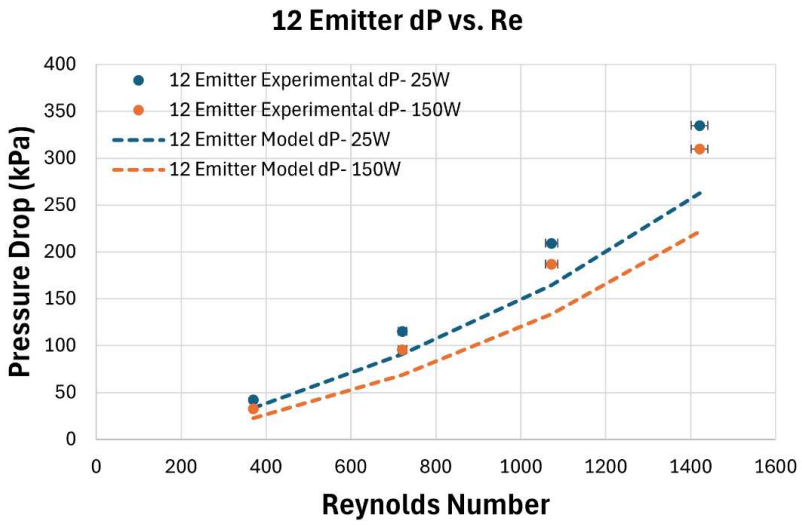

Figure 5-8- 12-emitter test section simulation and experimental comparison of pressure drop across the microchannels across all the tested flow rates, at the lowest and highest heat load.

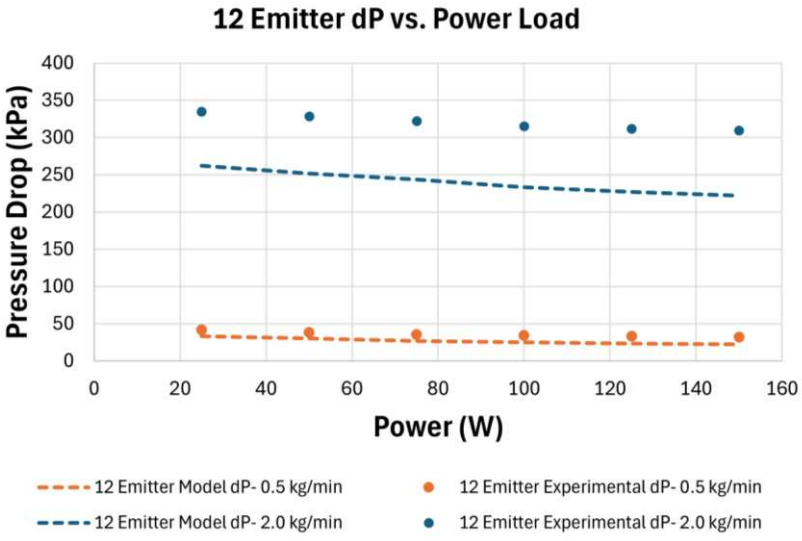

Figure 5-9- 12-emitter test section simulation and experimental comparison of pressure drop across the microchannels across all the power loads tested, at the lowest and highest flow rate.

5.3. Axial Pressure Drop

As previously mentioned, it is possible that there is some laminar to turbulent transitional flow behavior occurring in the channels at higher flow rates. This can be seen in Figure 5-10 and Figure 5-11. Figure 5-10 displays the pressure drop along the length of the channels for the broad

area model at the 0.5 kg/min conditions. One can see the large initial pressure drop that occurs as the fluid passes from the plenum region into the microchannels, followed by a roughly linear pressure drop within the channels. It is important to note the increasingly large proportion of the pressure drop occurring from that inlet plenum region at the flow rate increases. The flow transitions need to be captured accurately within this region in order to accurately predict the overall pressure drop. There is a slight curve at the beginning of the pressure drop in the channels which is a characteristic of developing flow. Figure 5-11 displays the same image but for the 2 kg/min scenario. At the higher flow rate, there is a clear sign of possible turbulence in the channels following the initial pressure drop from the plenum. This can be due to the formation of eddies in the microchannel which would cause that slight pressure recovery.

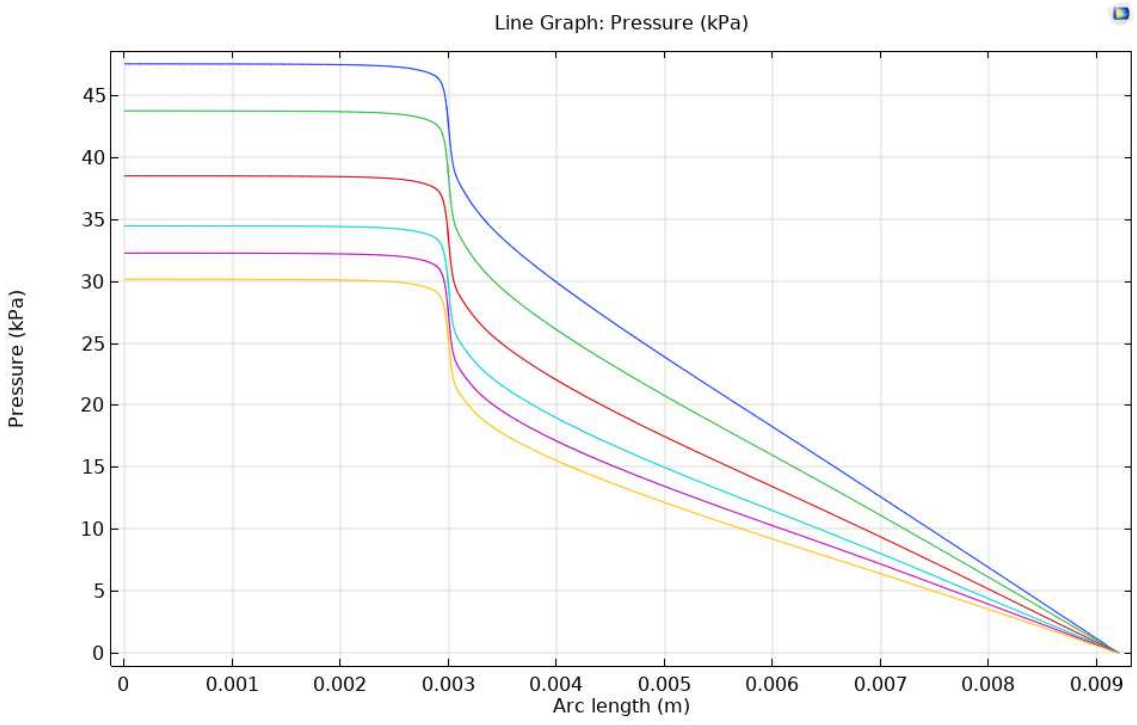

Figure 5-10- Axial pressure drop observed in the broad area model at 0.5 kg/min at every heat load.

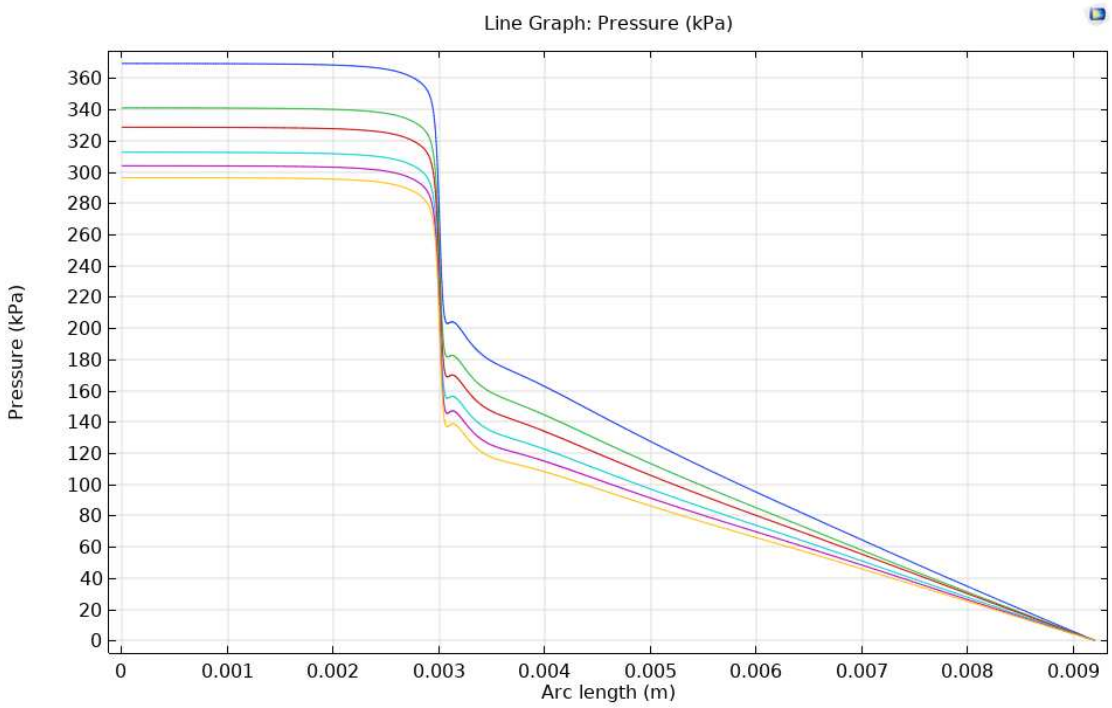

Figure 5-11- Axial pressure drop observed in the broad area model at 2 kg/min at every heat load.

Figure 5-12 displays the experimental pressure drop at 150W for each test section versus the friction factor pressure drop for each test section at 150W. These values are calculated using the following equations:

$$f = \frac{96}{Re}(1 - 1.3553\beta + 1.9467\beta^2 - 1.7012\beta^3 + 0.9564\beta^4 - 0.2537\beta^5) \quad (13)$$

$$\Delta P_f = \frac{1}{2\rho}\left(\frac{\dot{m}}{A_{ch}N_{ch}}\right)^2 \frac{f L_{ch}}{D_h} \quad (14)$$

where $\beta = \frac{W_{ch}}{H_{ch}}$. Similar to the model predictions, the fiction factor pressure drop is substantially lower than the experimental pressure drop. As mentioned above, there are several additional sources of pressure drop experimentally that are not captured in the model or in the friction factor pressure drop correlation such as the fluid flow behavior. The friction factor pressure drop calculation assume fully developed flow, and the contraction losses into the channels as well as

the developing flow start to become more dominant at higher flow rates where the pressure drop starts to deviate more from the fully developed frictional pressure drop line

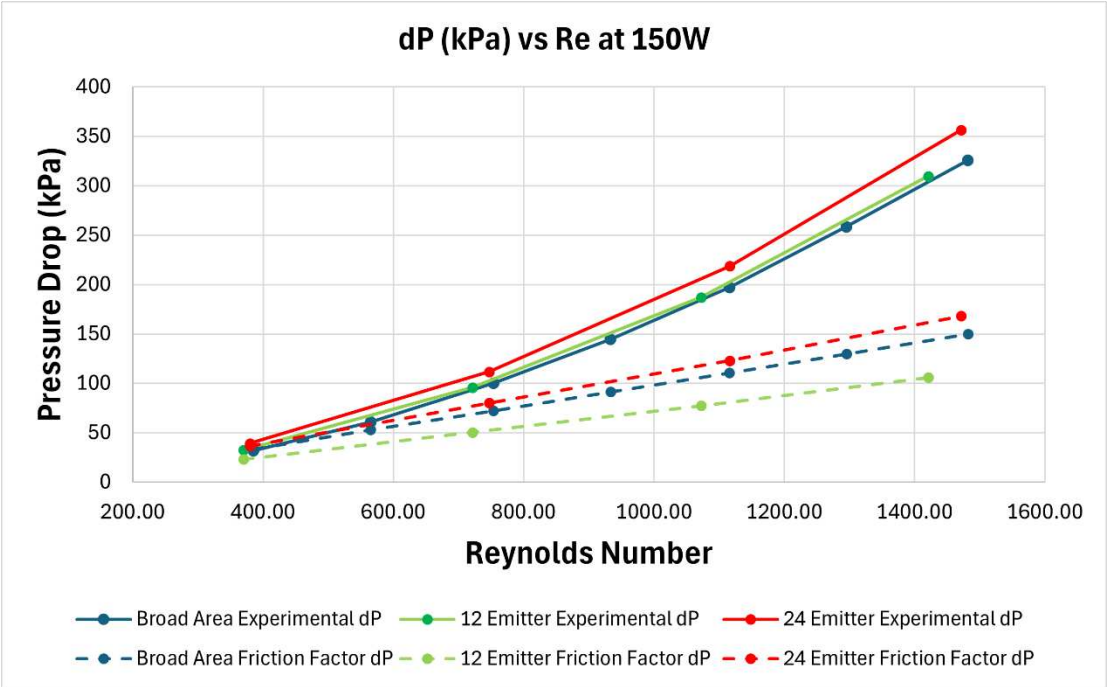

Figure 5-12- Experimental pressure drop at 150W vs. friction factor pressure drop at 150W.

5.4. Fluid Flow Behaviors

Figure 5-13 shows the cross-sectionally averaged velocity observed in the broad area model at 2 kg/min at every heat load. The flow velocity starts out small and increases as it enters the channel. One can also see the short developing region followed by a large majority of the channel of fully developed flow. Figure 5-14 and Figure 5-15 display the flow velocity profile in the channels of the broad area unit cell model at the lowest and highest flow rates tested and at 150W. By comparing these two figures, one can see the longer developing region in the channels at higher flow rates and the development of turbulent conditions at higher flow rates in the form of possible eddies. This could be attributed to the large step profile created from the inlet manifold

area. The large step-down area could result in eddies being formed at the channel inlet and would result in a larger pressure drop. These flow conditions could be improved by angling the manifold inlet area so that there is a smoother flow transition into the channels.

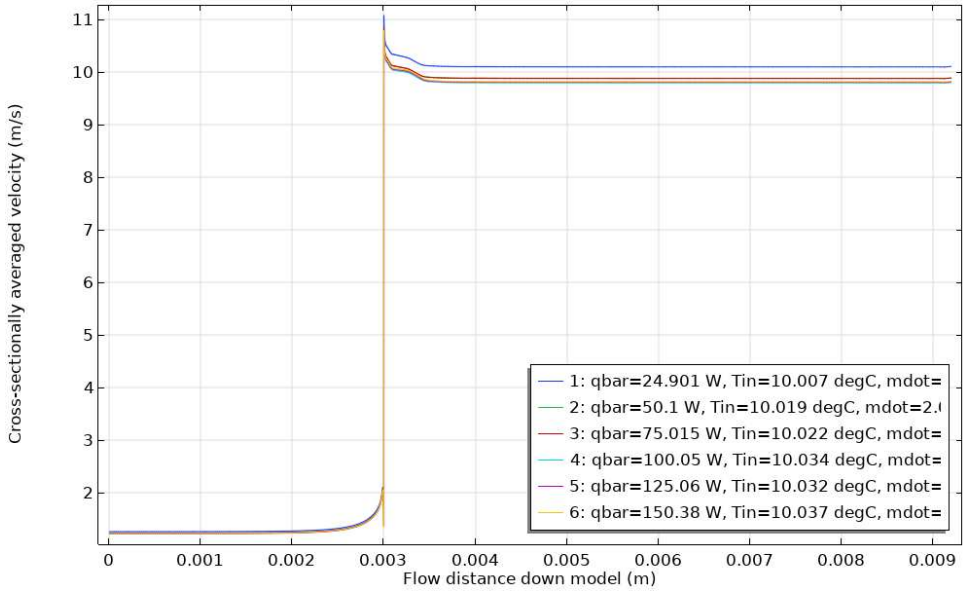

Figure 5-13- Cross-sectionally averaged velocity observed in the broad area model at 2 kg/min at every heat load.

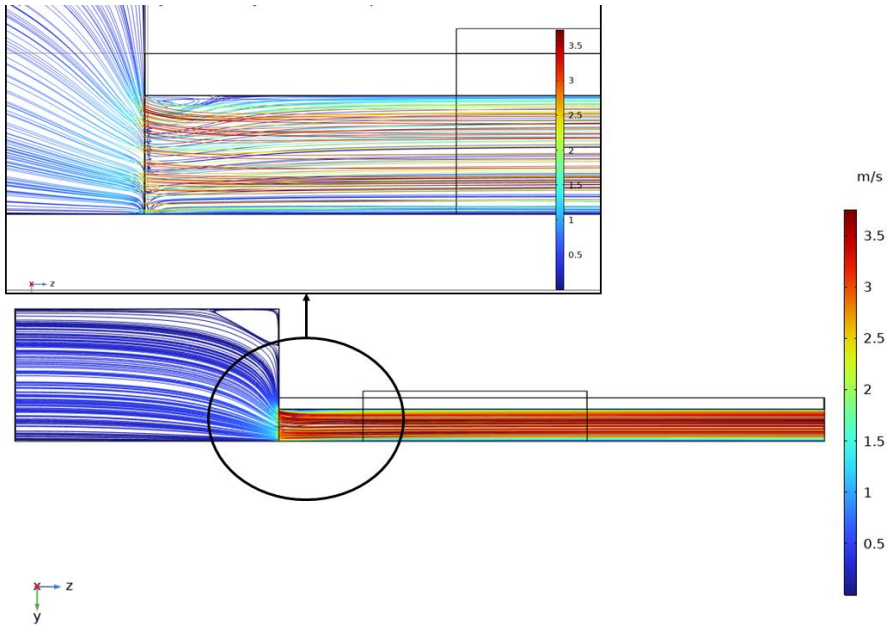

Figure 5-14- Flow velocity profile in the broad area model at 0.5 kg/min and 150W.

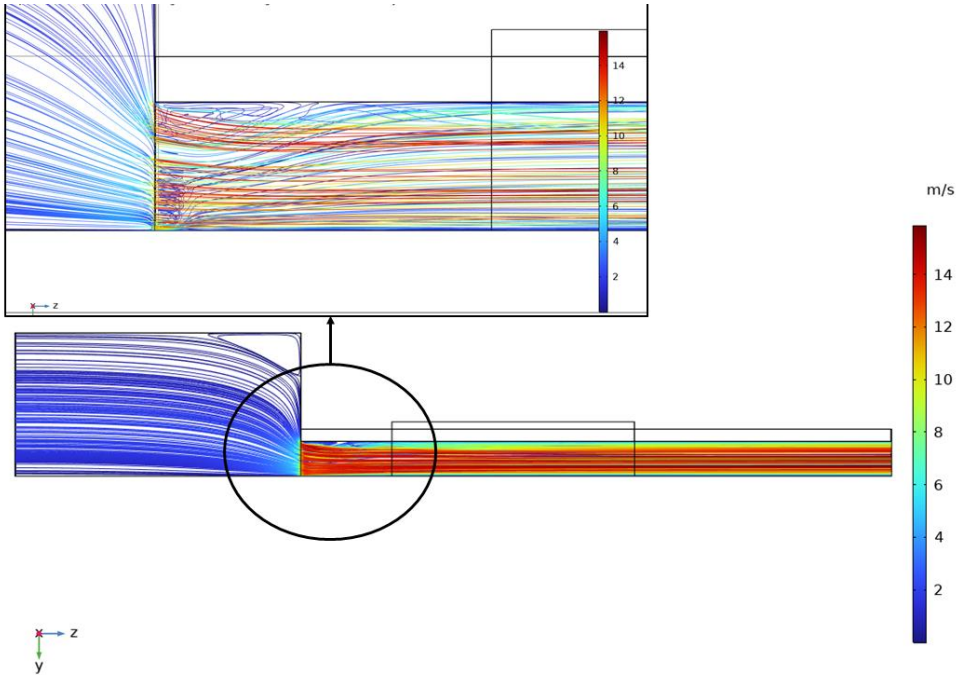

Figure 5-15- Flow velocity profile in the broad area model at 2 kg/min and 150W.

5.5. Temperature Comparison

Figure 5-16 shows the solid models for all three test sections displaying the resulting temperatures for a flow rate of 2 kg/min and heat flus of 150W. This was the highest flow rate and highest heat load tested. This graph is made by mirroring the unit cell model several times until it represents the full length of the heater. One can clearly see the discrete emitters for the 12-emitter and 24-emitter test sections and these “emitters” are meant to act as surrogate laser diodes, effectively representing the temperature distribution of a laser diode bar.

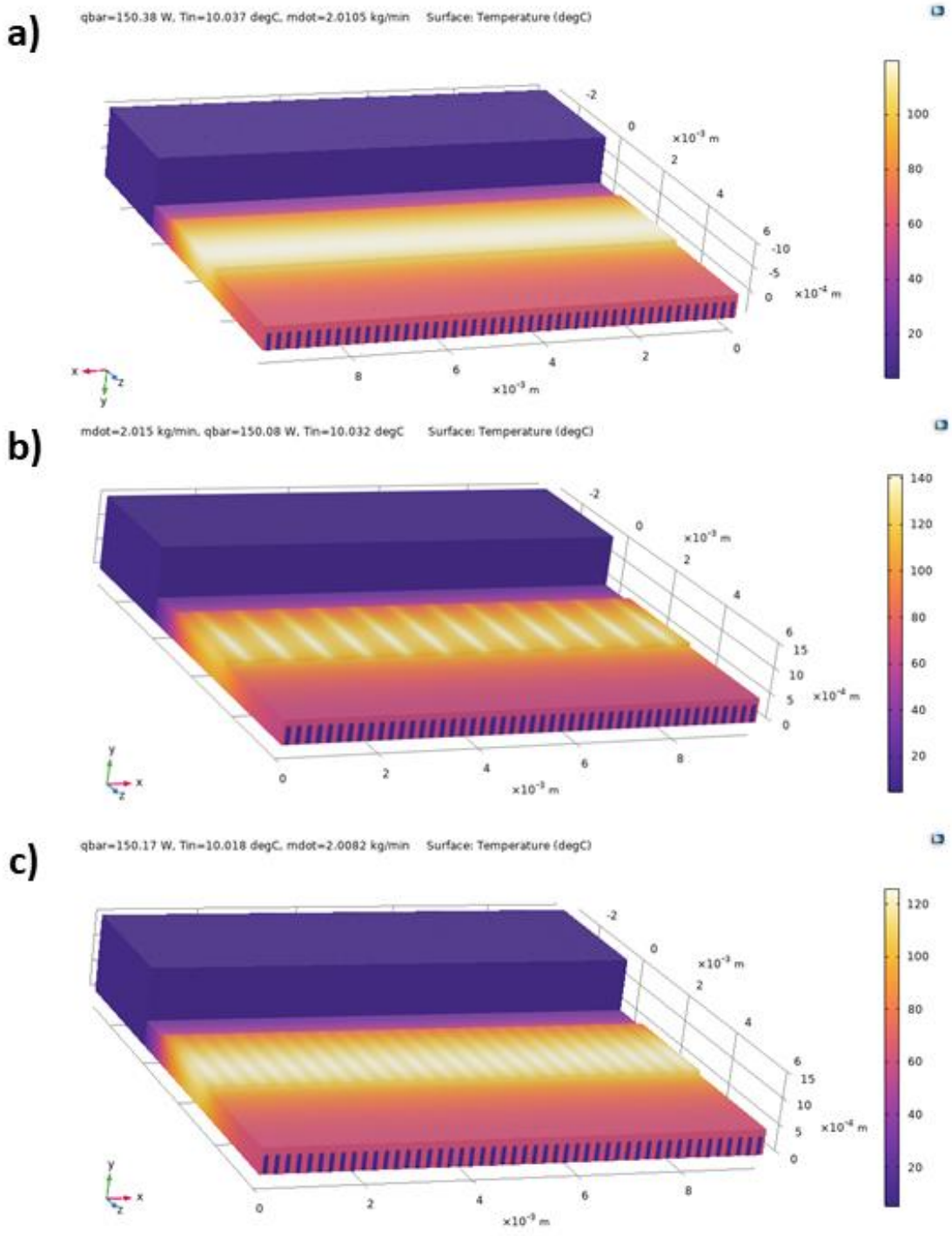

Figure 5-16- a) Mirrored solid model displaying the temperature across the broad area test section. b) Mirrored solid model displaying the temperature across the 12 emitter test section. c) Mirrored solid model displaying the temperature across the 24 emitter test section.

Figure 5-17 shows the horizontal temperature distribution across each of these images, 1.75 mm downstream from the heaters edge, which roughly coincides with the peak temperature location observed on the heater. Although this does not fully represent the temperature behavior in the horizontal direction, normal to the flow direction, it gives a clear visualization of what the temperature distribution looks like across different heater designs. This figure shows the importance of considering discrete emitter heaters because the heat transfer, and thus the temperature, can vary significantly across the peaks and troughs. This provides a simulation of what might occur in real laser emitters to further understand the best cooling approach. It is important to note that these lines would begin to drop on both sides of the graph due to additional heat spreading into the peripheral sidewalls of the device that are not modeled here.

The 12-emitter is expected to have the highest average heater temperature and highest peak to trough variation due to the higher heat flux observed in each emitter, followed by the 24-emitter test section, and finally the broad area test section. This is consistent with the observed horizontal temperature distribution. This can also be seen in the experimental results in Figure 5-18, which shows both the experimental and numerical average heater temperature for the 150W scenario for each test section at varying flow rates. Due to the heater geometry, the broad area test section and the 24-emitter test sections behave very similarly to each other which explains the comparable average heater temperatures. This also displays the relative accuracy of using a broad area approach, which is more accurate when you have a larger number of emitters spaced more closely. Fewer emitters spaced further apart increases the heat flux for each emitter and results in a more enhanced peak-and-trough profile. It is important to note that all three test sections all have slightly different channel geometries which makes them difficult to fully compare.

One can note that the model is overpredicting the average heater temperature in Figure 5-18 at the lowest flow rate. This can be due to possible deviation from the average heater temperature curve fit. The electrical resistance calibration was performed from 18°C to 95°C and the average heater temperatures at those lower flow rates are significantly higher than 95°C. Additionally, there could be substantial lateral heat spreading into the contact pad side walls and the spacing in between the emitters. The 12-emitter test section has the largest difference between experimental results and model prediction and one explanation is due to the nature of the heater design, there is a larger side substrate and additional channels in areas with no heating resulting in additional heat spreading and a lower average heater temperature. It is possible the unit cell model approach might be less applicable for the 12-emitter test section.

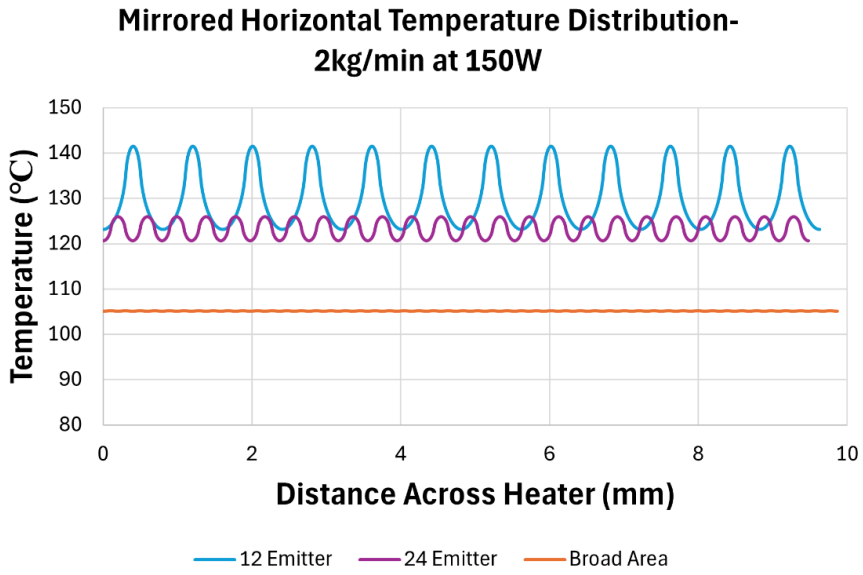

Figure 5-17- Simulated horizontal temperature distribution across each test section.

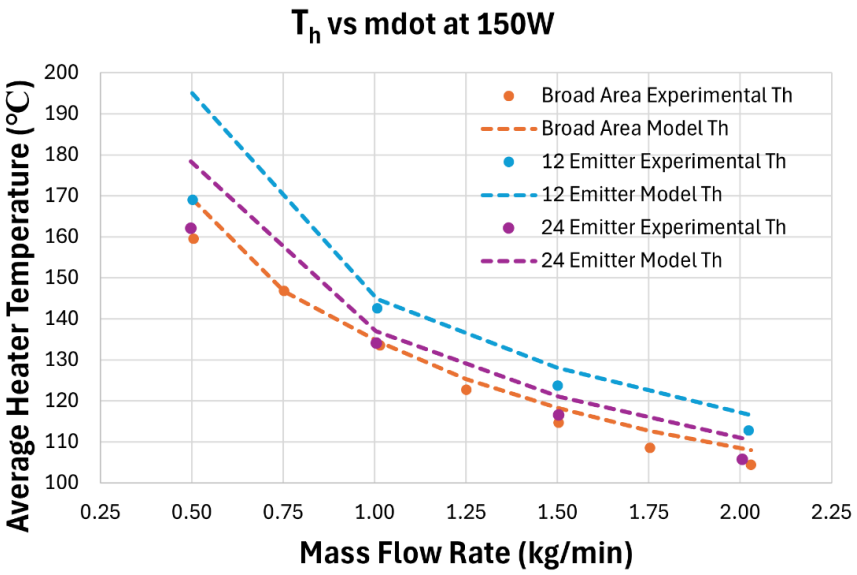

Figure 5-18- Comparison of simulation and experimental average heater temperatures across every tested flow rate, for each test section, at the highest applied heat load.

5.5.1. Axial Heat Transfer Coefficient

Figure 5-19 displays the heat transfer coefficient values along the length of the channels (averaged across all three sides of the channel) for all heat loads tested. This is plotted for the 2 kg/min, 1 kg/min and 0.5 kg/min scenarios for the broad area unit cell model. All three models behave similarly in terms of the overall trend experienced along the channels. The heat transfer coefficient is initially very high at the inlet due to the thinness of the thermal boundary layer and is followed by a flow recovery or recirculation effect which is seen as a brief and sudden increase in heat transfer coefficient. From there, the heat transfer coefficients gradually decrease in the area prior to the heater and directly underneath the heater, which is the developing region. In the channel area past the heater, the heat transfer coefficients decay quickly and flatten out meaning that additional length of the channels is no longer contributing much to the heat transfer. This means that a large majority of the channel length past the heater is simply causing a larger pressure drop

across the channels. Using shorter channels in the future would result in similar performance without the penalty of a large pressure drop at the higher flow rates.

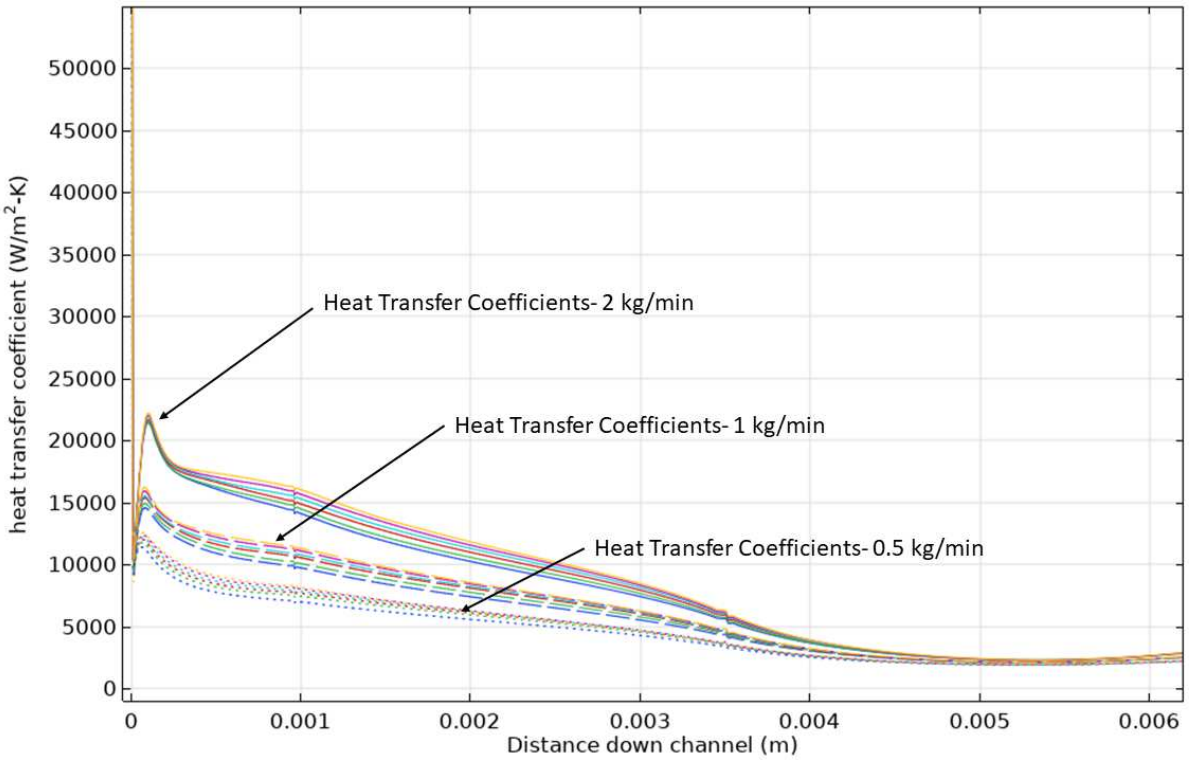

Figure 5-19- Heat transfer coefficients along the length of the channel for the broad area heater at various heat loads and flow rates.

5.6. Thermal Resistance

Figure 5-20 displays the resulting thermal resistances (R_{th}) versus the Reynolds numbers tested for each test section and compares the experimental results to the simulation predictions. If the geometries were the same across all test sections, the discrete emitters should have a higher average temperature resulting in a higher R_{th}, because the heat is concentrated in smaller areas resulting in a higher heat flux. In agreement with this hypothesis, the 12-emitter test section exhibits the highest heat flux which reflects the resulting higher thermal resistance, followed by the 24-emitter and lastly the broad area emitter which has the lowest thermal resistance. It is important to note the clear difference between assuming a uniformly distributed heat load and

using a discrete approach. There is an increasing interest in using microchannel coolers for cooling next-generation laser diode arrays, and it is important to consider the higher heat fluxes that occur in the discretized heat sources which results in higher thermal resistances. The lowest thermal resistance achieved experimentally was 0.15 cm^2 K/W for the broad area test section at 2 kg/min and the highest experimental thermal resistance observed was 0.26 cm^2 K/W for the 12-emitter test section at 0.5 kg/min. As expected, the R_{th} curve begins to asymptote as the Reynolds numbers increases. When higher flow rates are reached, the convective thermal resistance decreases until it eventually approaches the conduction-limited thermal resistance. This is caused by larger temperature gradients resulting in greater heat transfer coefficients due to the smaller boundary layer thickness at higher flow rates.

The previous study performed by Cassada et al. [38] used different channel geometries and materials but had the same size heater footprint. The comparison of the broad area thermal resistance calculated in this study and from Cassada et al. is plotted versus each of the tested flow rates in Figure 5-21. It is difficult to compare these two experimental studies as there is a large difference in the microchannel geometry and in the material and fluid properties. The thermal resistances from the current study are significantly higher than that found in Cassada et al. [38] and this is clearly attributed to the larger microchannels, microchannel material properties, and the fluid used in this study.

Using wider microchannels for this study resulted in a reduced surface area and the dielectric fluid used has a much lower thermal conductivity compared to water. If the channels geometry was decreased substantially, for example to that used in Cassada's study, higher flow rates would lead to impractically large pressure drop values. Despite the higher thermal resistances found in this study, the results have been very informative for future studies exploring alternative

fluids and substrate materials for cooling GaAs diodes. Optimization of the MCHS geometry to increase the surface area and selecting a higher thermal conductivity dielectric fluid would greatly improve these results.

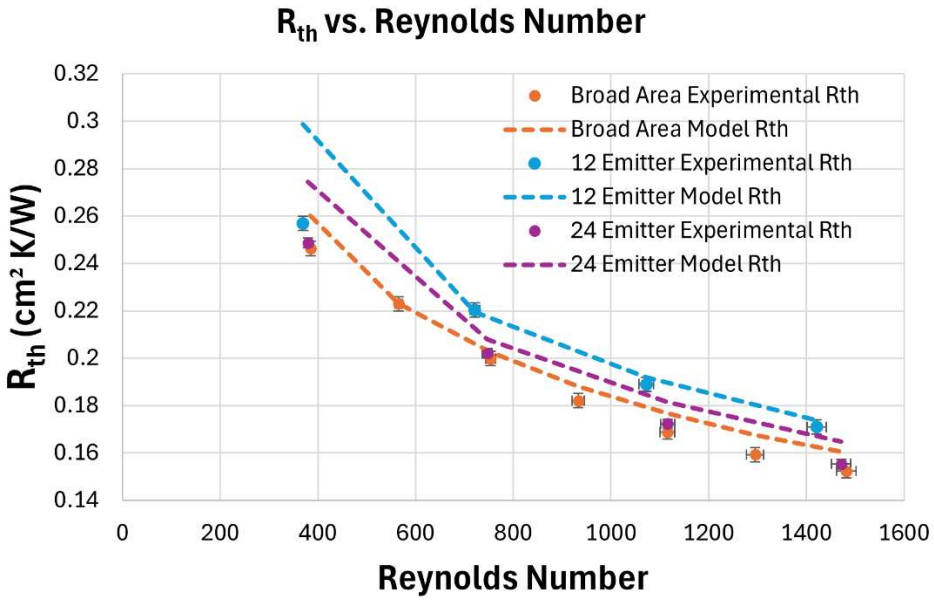

Figure 5-20- Simulation and experimental comparison of thermal resistance of each test section across various Reynolds numbers.

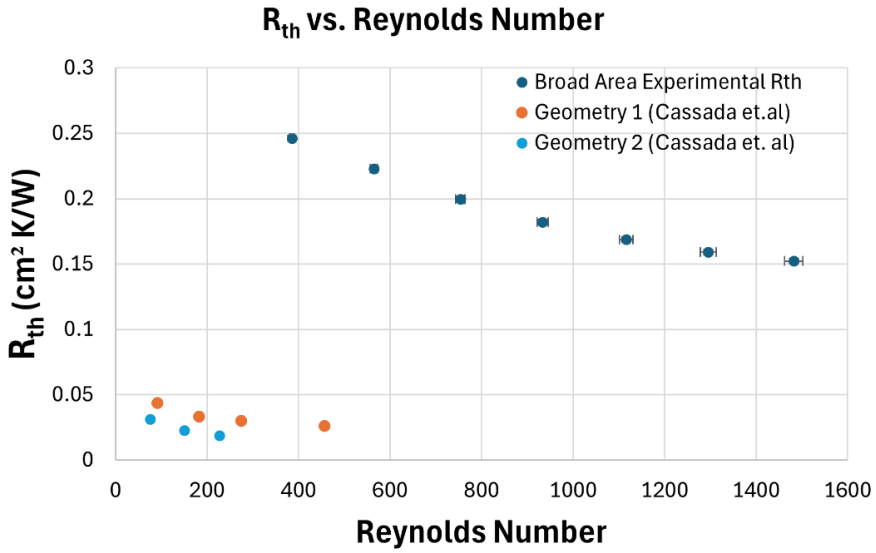

Figure 5-21- Broad area experimental thermal resistance compared to Cassada's study [38].

5.7. Alternate Geometry and Fluid

An additional model was created to investigate the impact a different fluid and smaller channels would have on the overall thermal performance. This model was created using the same MCHS materials as used in this study and the same inlet conditions as used in the previous models, but the channel geometry was changed to be comparable to Geometry 1 used in Cassada's study: 92 channels which were ~50 µm x 400 µm. The cooling fluid was also changed to HFE7200 (thermal conductivity: 0.068 W/m-K at 25 °C vs 0.064 W/m-K for FC3283 at the same temperature). The average temperature results can be seen in Figure 5-22 and the 2 kg/min temperature results are plotted against the FC3283 test and numerical results in Figure 5-23. The thermal performance using this fluid and geometry was far superior to using FC3283 and 100 µm wide channels from the current study. At the highest heat load, the heater temperature is roughly a 40 °C lower than the FC3283 results. This is a significant decrease in temperature which is far closer to the ~50°C limit that laser diode junctions must meet for optimal performance.

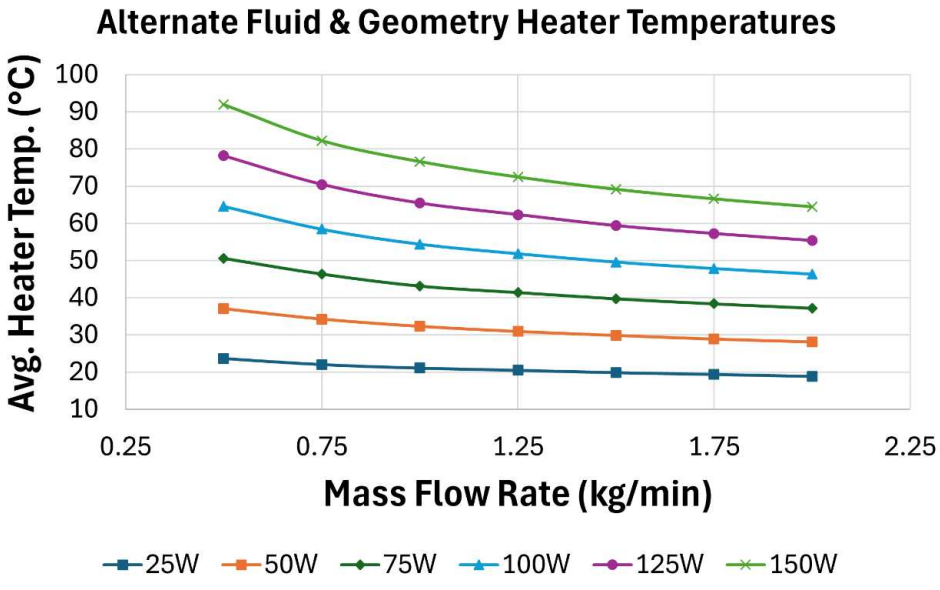

Figure 5-22- Average broad area heater temperature using HFE7200 as the cooling fluid and 50 µm wide channels at each power load for each flow rate.

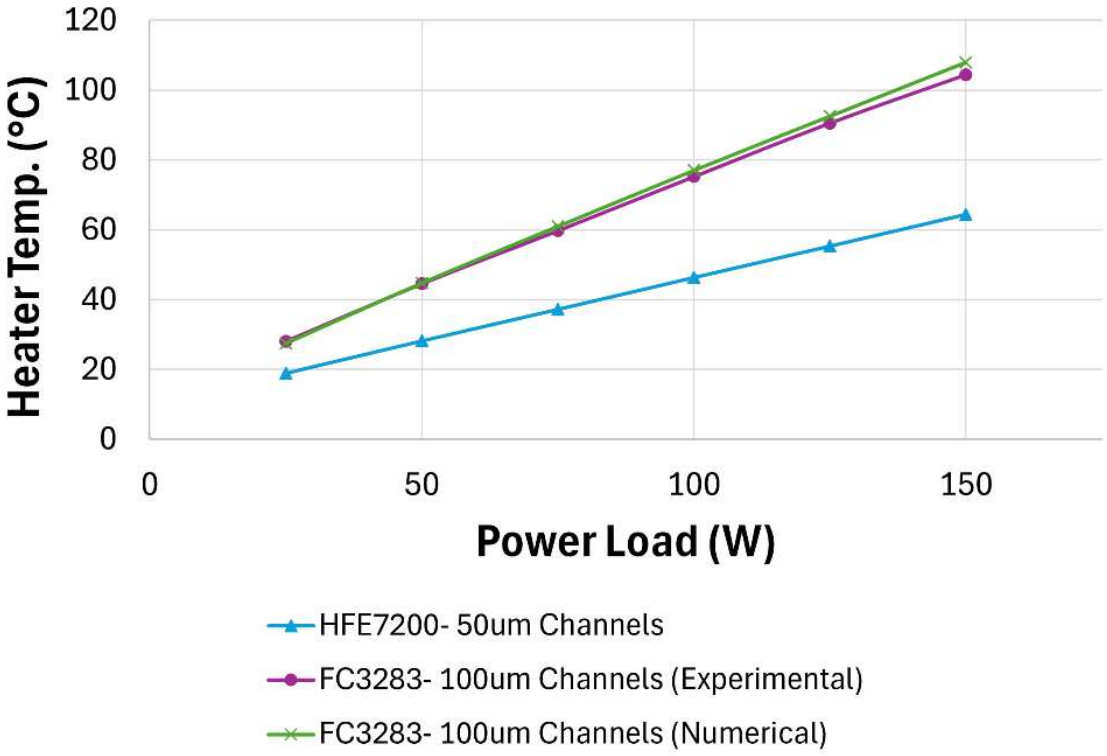

Figure 5-23- Broad area heater temperature comparison of HFE7200 model with 50 um wide channels to FC3283 test and model with 100 um wide channels, at 2 kg/min.

At 150 W and 2 kg/min, the pressure drop is about 375 kPa, and the average temperature is <65°C compared to a pressure drop of about 325 kPa, and an average temperature of ~105°C at the same conditions using FC3283 and 100 µm wide channels. Additionally, despite having narrower channels (roughly half the width), the pressure drop was comparable due to the lower viscosity fluid (0.58 cP vs. 1.4 cP for FC3283 at 25 °C). Figure 5-24 displays the comparison of the heat transfer coefficient values along the length of the channels for the HFE7200 model and the FC3283 model at 2 kg/min and 150 W. The HFE7200 model had significantly higher heat transfer coefficients which leads to the improved thermal performance. Figure 5-25 displays the comparison of the broad area thermal resistance of the HFE7200 model against the thermal resistances calculated in this study using FC3283 and from Cassada et al. is plotted versus each of the tested flow rates. Using a superior fluid and a smaller channel geometry with an increased

surface area, results in thermal resistances that are much lower than those found in this study and much closer to the results found in Cassada et al. [38]. It is important to note that the Reynolds values at the higher flow rates are in the transitional flow regime and the model was run using a laminar flow model. The transitional flow could have an impact on the overall results but the turbulent transition model in COMSOL is correlation based, and it is likely that it may not accurately represent when the transition begins, given the wide range in transition conditions observed in the literature. For this reason, the next step would be to experimentally validate those HFE results at the higher flow rates.

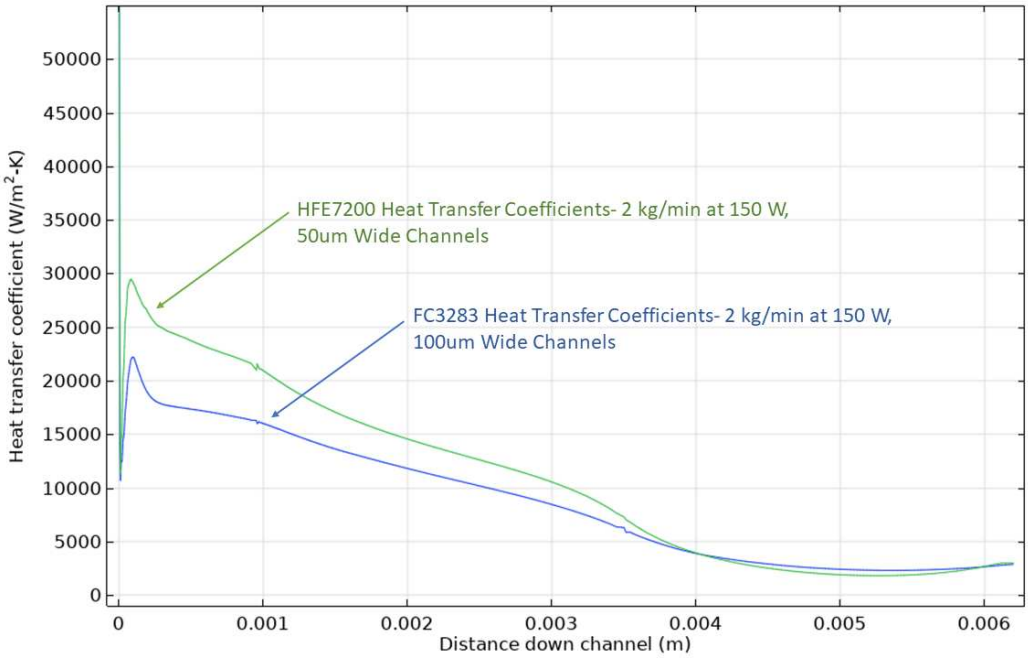

Figure 5-24- Comparison of FC3283 and HFE7200 heat transfer coefficients along the length of the channel for the broad area heater at 2 kg/min and 150 W.

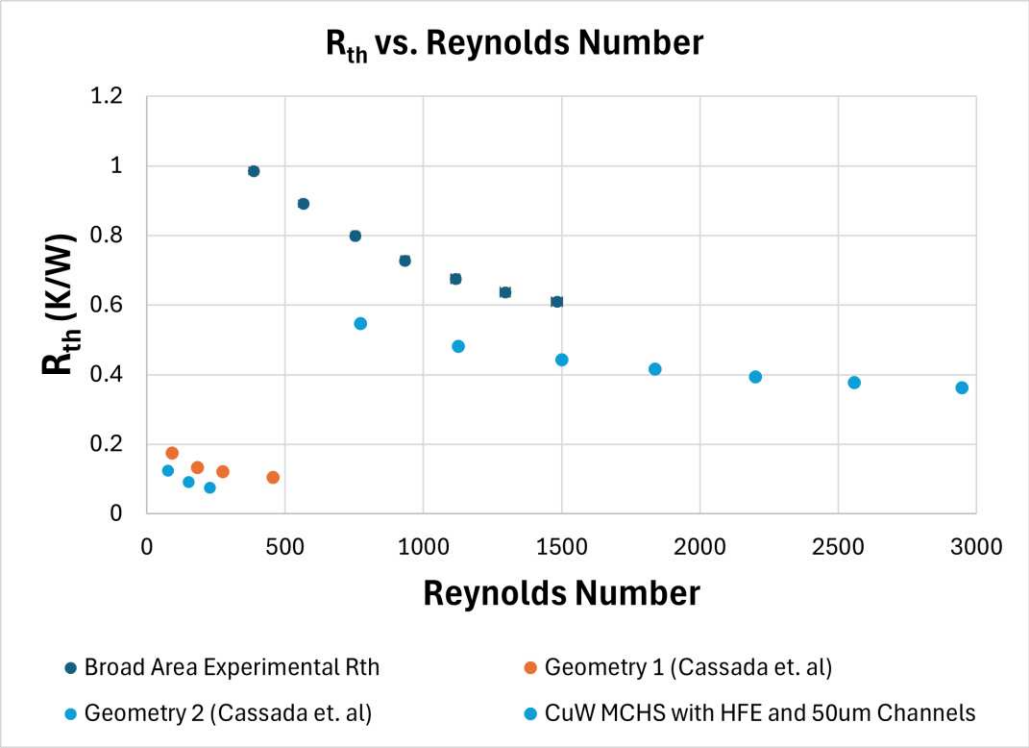

Figure 5-25- Broad area experimental thermal resistance compared to Cassada's study and to this HFE7200 model with 50 um wide channels.

CHAPTER 6. Conclusions and Recommendation for Further Work

The current study sought to understand if CuW microchannels can effectively dissipate high heat fluxes using FC3283. This work explored three different distributions of high heat fluxes in the aim of creating a heater that is representative of a laser diode bar. The different heater designs consisted of a singular uniformly distributed heater and discretized heaters, using a dielectric fluid as the cooling fluid. This work reported on the experimental and numerical findings of each of the different heater designs using CuW microchannels with FC3283. Experimental studies tested a variety of power loads and flow rates, and the results of each test section were validated using a unit cell model created in COMSOL. The resulting heater temperatures from the models were within 4% of the experimental results at the highest flow rate and highest heat load for all three test sections. The experimental thermal resistances ranged from 0.15 cm^2 K/W for the broad area test section at the highest flow rate to 0.26 cm^2 K/W for the 12-emitter test section at the lowest flow rate.

This study was the first to explore the unique combination of CuW microchannels and FC3283 as the cooling fluid. The distinctive combination of using an electrically conductive CuW substrate, which is thermal-expansion matched to typical laser diode substrate materials, with a low resistivity, dielectric fluid such as FC3283, provides a practical cooling approach for laser diode applications such as, multi-bar GaAs laser diode stacks. Reasonable agreement was found between the numerical model and the experimental results. The resulting thermal performance from this study proved to be insufficient for maintaining optimal temperatures for laser diode applications. Additional model results show that device performance can be improved in the future by optimizing the geometry, operating at higher flow rates, and using substrate or dielectric fluids

with higher thermal conductivities. This study reviled the importance of considering discrete heat sources separately from uniform heat sources and proved that CuW microchannels can be a promising cooling option toward future advancements of laser diode bars and other high-power microelectronics when using a low viscosity and high thermal conductivity, dielectric cooling fluid and an optimized geometry. Furthermore, the predictive capabilities of the model can be improved by accounting for transitional and turbulent flow behavior. Overall, this study demonstrates a promising pathway for cooling high-power electronics and, most importantly, provides a unique MCHS compatible with laser diode applications.

6.1. Recommendations for Future Work

There are a few items that should be investigated further. The three key parts of the future work for this study are as follows:

- Channel optimization is the clear next step for thermal performance improvement. This work consisted of a proof-of-concept study which was successfully completed. In the future, these results can be improved tremendously by performing a channel optimization study. This will ensure that the thermal performance is at the maximum efficiency possible while maintaining a manageable pressure drop throughout the channels. It would also be beneficial to investigate how different emitter widths and pitches could possibly require different optimal fin and channel dimensions as well as material floor thickness. As seen in this work, it is important to consider how different temperature distributions can impact the thermal dissipation through MCHS. Different heater geometries could have different optimized channel geometries.
- Further exploration of alternate fluids is another key area that can have a tremendous impact on the thermal performance of the CuW MCHS for laser diode applications. As

shown in section 5.7, the thermal results were greatly improved by using HFE7200. This fluid has a comparable thermal conductivity but has a significantly lower viscosity than FC3283 which resulted in an improved performance because facilitated the use of narrower channels and higher flow rates with reduced pressure drop. Choosing fluids with a similar viscosity as HFE7200 but with a higher thermal conductivity, would further improve performance. Fluids with a higher specific heat would allow lower flow rates to be used for a given fluid temperature gradient and would also facilitate the use of narrower channels.

- CuW proved to be an acceptable material for MCHS but there is a possibility of improving the overall thermal performance by using a MCHS with a higher thermal conductivity. The previous study performed by Cassada [38] used SiC which had a significantly higher thermal conductivity. The study found a lower thermal conductivity than using CuW microchannels, but it is unclear if the MCHS with superior thermal conductivity had as big as an impact on the improved performance as the superior fluid used in that study (water). It is important to investigate the impact of the MCHS material as well as the cooling fluid and determine which has the greatest effect on the overall thermal performance.
- The fluid flow field can be further improved by modifying the manifold design to ensure a smoother transition from the plenum region into the channels. Optimizing the manifold design could be just as important as optimizing the channel geometry as it can have a large impact on the flow behavior. One must have a complete understanding of the possible flow behaviors occurring experimentally to make certain the model is assuming the proper boundary conditions and ensure proper model validation.

REFERENCES

[1] D. B. Tuckerman and R. F. W. Pease, "High-Performance Heat Sinking for VLSI," *IEEE Electron Device Letters*, vol. EDL-2, no. 5, 1981, doi: 10.1109/EDL.1981.25367.

[2] W. Qu and I. Mudawar, "Experimental and numerical study of pressure drop and heat transfer in a single-phase micro-channel heat sink," *Int J Heat Mass Transf*, vol. 45, no. 12, 2002, doi: 10.1016/S0017-9310(01)00337-4.

[3] S. Weaver *et al.*, "Experimental development of a near junction microchannel heat spreader," in *Thermomechanical Phenomena in Electronic Systems -Proceedings of the Intersociety Conference*, 2014. doi: 10.1109/ITHERM.2014.6892386.

[4] T. M. Bandhauer and T. A. Bevis, "High heat flux boiling heat transfer for laser diode arrays," in *ASME 2016 14th International Conference on Nanochannels, Microchannels, and Minichannels, ICNMM 2016, collocated with the ASME 2016 Heat Transfer Summer Conference and the ASME 2016 Fluids Engineering Division Summer Meeting*, 2016. doi: 10.1115/ICNMM2016-7947.

[5] M. Pospiech and S. Liu, "Laser Diodes: An Introduction," University of Hannover.

[6] M. Leers and K. Boucke, "Cooling approaches for high power diode laser bars," in *Proceedings - Electronic Components and Technology Conference*, 2008. doi: 10.1109/ECTC.2008.4550100.

[7] J. A. Skidmore *et al.*, "Silicon monolithic microchannel-cooled laser diode array," *Appl Phys Lett*, vol. 77, no. 1, 2000, doi: 10.1063/1.126860.

[8] "photonics.com."

[9] I. A. Ghani, N. A. Che Sidik, N. Kamaruzzaman, W. Jazair Yahya, and O. Mahian, "The effect of manifold zone parameters on hydrothermal performance of micro-channel

HeatSink: A review," *International Journal of Heat and Mass Transfer*, vol. 109. 2017. doi: 10.1016/j.ijheatmasstransfer.2017.03.007.

[10] R. Zhang, M. Hodes, N. Lower, and R. Wilcoxon, "Water-based microchannel and galinstan-based minichannel cooling beyond 1 kw/cm2 heat flux," *IEEE Trans Compon Packaging Manuf Technol*, vol. 5, no. 6, 2015, doi: 10.1109/TCPMT.2015.2426791.

[11] L. Zhang, B. Jones, F. Buja, V. Cherman, H. Oprins, and P. Soussan, "High Heat Flux Removal Using Optimized Microchannel Heat Sink," in *THERMINIC 2018 - 24th International Workshop on Thermal Investigations of ICs and Systems, Proceedings*, 2018. doi: 10.1109/THERMINIC.2018.8593328.

[12] G. Mandrusiak *et al.*, "Engineering design of a near junction thermal transport heat spreader," in *Technical Digest - IEEE Compound Semiconductor Integrated Circuit Symposium, CSIC*, 2012. doi: 10.1109/CSICS.2012.6340097.

[13] E. G. Colgan *et al.*, "A practical implementation of silicon microchannel coolers for high power chips," *IEEE Transactions on Components and Packaging Technologies*, vol. 30, no. 2, 2007, doi: 10.1109/TCAPT.2007.897977.

[14] D. R. S. Raghuraman, R. Thundil Karuppa Raj, P. K. Nagarajan, and B. V. A. Rao, "Influence of aspect ratio on the thermal performance of rectangular shaped micro channel heat sink using CFD code," *Alexandria Engineering Journal*, vol. 56, no. 1, 2017, doi: 10.1016/j.aej.2016.08.033.

[15] L. C. Joshi, S. Singh, and S. R. Kumar, "A review on enhancement of heat transfer in microchannel heat exchanger," *International Journal of Science Engineering & Technology*, vol. 1, no. 9, 2014.

[16] V. K. Samalam, “Convective heat transfer in microchannels,” *J Electron Mater*, vol. 18, no. 5, 1989, doi: 10.1007/BF02657475.

[17] R.J. Phillips, “Micro-channel heat sinks,” *Advances in Thermal Modeling of Electronic Component*, vol. 2, pp. 109–184, 1990.

[18] J. S. G. D. J. H. R.W. Knight, “Optimal Thermal Design of Forced Convection Heat Sinks – Analytical,” *ASME J. Electron. Packaging 113*, pp. 313–321, 1991.

[19] R. W. Knight, J. S. Goodling, D. J. Hall, and R. C. Jaeger, “Heat Sink Optimization with Application to Microchannels,” *IEEE Transactions on Components, Hybrids, and Manufacturing Technology*, vol. 15, no. 5, 1992, doi: 10.1109/33.180049.

[20] A. Bejan and A. M. Morega, “Optimal arrays of pin fins and plate fins in laminar forced convection,” *J Heat Transfer*, vol. 115, no. 1, 1993, doi: 10.1115/1.2910672.

[21] D. Y. Lee and K. Vafai, “Comparative analysis of jet impingement and microchannel cooling for high heat flux applications,” *Int J Heat Mass Transf*, vol. 42, no. 9, 1999, doi: 10.1016/S0017-9310(98)00265-8.

[22] F. Buja, L. Zhang, V. Cherman, H. Oprins, B. Jones, and P. Soussan, “High heat flux dissipation via interposer active micro-cooling,” *Jpn J Appl Phys*, vol. 58, no. SB, 2019, doi: 10.7567/1347-4065/ab002d.

[23] G. Xia, D. Ma, Y. Zhai, Y. Li, R. Liu, and M. Du, “Experimental and numerical study of fluid flow and heat transfer characteristics in microchannel heat sink with complex structure,” *Energy Convers Manag*, vol. 105, 2015, doi: 10.1016/j.enconman.2015.08.042.

[24] L. J. Missaggia, J. N. Walpole, Z. L. Liau, and R. J. Phillips, “Microchannel Heat Sinks For Two-Dimensional High-Power-Density Diode Laser Arrays,” *IEEE J Quantum Electron*, vol. 25, no. 9, 1989, doi: 10.1109/3.35223.

[25] S. K. Roy and B. L. Avanic, “A very high heat flux microchannel heat exchanger for cooling of semiconductor laser diode arrays,” *IEEE Transactions on Components Packaging and Manufacturing Technology Part B*, vol. 19, no. 2, 1996, doi: 10.1109/96.496049.

[26] J. S. Goodling, “Microchannel Heat Exchangers: A Review,” *Proceedings of High Heat Flux Engineering II*, pp. 66–82, 1997.

[27] C. B. Sobhan and S. V. Garimella, “A comparative analysis of studies on heat transfer and fluid flow in microchannels,” *Microscale Thermophysical Engineering*, vol. 5, no. 4, 2001, doi: 10.1080/10893950152646759.

[28] B. Palm, “Heat Transfer in Microchannels,” *Microscale Thermophysical Engineering*, vol. 5, no. 3, pp. 155–175, 2001.

[29] Z. Y. Guo and Z. X. Li, “Size effect on single-phase channel flow and heat transfer at microscale,” *Int J Heat Fluid Flow*, vol. 24, no. 3, 2003, doi: 10.1016/S0142-727X(03)00019-5.

[30] G.L. Morini, “Single-phase convective heat transfer in microchannels: a review of experimental results,” *International Journal of Thermal Sciences*, pp. 631–651, 2004.

[31] B. Agostini, M. Fabbri, J. E. Park, L. Wojtan, J. R. Thome, and B. Michel, “State of the art of high heat flux cooling technologies,” *Heat Transfer Engineering*, vol. 28, no. 4, 2007, doi: 10.1080/01457630601117799.

[32] S. G. Kandlikar *et al.*, “Heat transfer in microchannels - 2012 status and research needs,” *J Heat Transfer*, vol. 135, no. 9, 2013, doi: 10.1115/1.4024354.

[33] M. Asadi, G. Xie, and B. Sunden, “A review of heat transfer and pressure drop characteristics of single and two-phase microchannels,” *International Journal of Heat and Mass Transfer*, vol. 79. 2014. doi: 10.1016/j.ijheatmasstransfer.2014.07.090.

[34] S. V. Ekkad and P. Singh, “Recent advancements in single-phase liquid-based heat transfer in microchannels,” in *Advances in Heat Transfer*, vol. 55, 2023. doi: 10.1016/bs.aiht.2022.12.001.

[35] T. M. Harms, M. J. Kazmierczak, and F. M. Gerner, “Developing convective heat transfer in deep rectangular microchannels,” *Int J Heat Fluid Flow*, vol. 20, no. 2, 1999, doi: 10.1016/S0142-727X(98)10055-3.

[36] P. S. Lee, J. C. Ho, and H. Xue, “Experimental study on laminar heat transfer in microchannel heat sink,” in *InterSociety Conference on Thermal and Thermomechanical Phenomena in Electronic Systems, ITHERM*, 2002. doi: 10.1109/ITHERM.2002.1012481.

[37] R. H. W. Pijnenburg, R. Dekker, C. C. S. Nicole, A. Aubry, and E. H. E. C. Eummelen, “Integrated micro-channel cooling in silicon,” in *ESSCIRC 2004 - Proceedings of the 34th European Solid-State Device Research Conference*, 2004. doi: 10.1109/essder.2004.1356506.

[38] N. Cassada *et al.*, “SiC Microchannel Heat Sinks for High Heat Flux Dissipation of 1 kW/cm2,” *IEEE Trans Compon Packaging Manuf Technol*, vol. 13, no. 5, 2023, doi: 10.1109/TCPMT.2023.3281772.

[39] P. S. Lee, S. V. Garimella, and D. Liu, “Investigation of heat transfer in rectangular microchannels,” *Int J Heat Mass Transf*, vol. 48, no. 9, 2005, doi: 10.1016/j.ijheatmasstransfer.2004.11.019.

[40] D. Liu and S. V. Garimella, “Investigation of liquid flow in microchannels,” *J Thermophys Heat Trans*, vol. 18, no. 1, 2004, doi: 10.2514/1.9124.

[41] Y. Liu, G. Xu, J. Sun, and H. Li, "Investigation of the roughness effect on flow behavior and heat transfer characteristics in microchannels," *Int J Heat Mass Transf*, vol. 83, 2015, doi: 10.1016/j.ijheatmasstransfer.2014.11.060.

[42] Y. Q. Xie, J. Z. Yu, and Z. H. Zhao, "Experimental investigation of flow and heat transfer for the ethanol-water solution and FC-72 in rectangular microchannels," *Heat and Mass Transfer/Waerme- und Stoffuebertragung*, vol. 41, no. 8, 2005, doi: 10.1007/s00231-004-0589-2.

[43] W. Qu and I. Mudawar, "Analysis of three-dimensional heat transfer in micro-channel heat sinks," *Int J Heat Mass Transf*, vol. 45, no. 19, 2002, doi: 10.1016/S0017-9310(02)00101-1.

[44] M. M. Rahman, "Measurements of heat transfer in microchannel heat sinks," *International Communications in Heat and Mass Transfer*, vol. 27, no. 4, 2000, doi: 10.1016/S0735-1933(00)00132-9.

[45] M. Hodes, R. Zhang, L. S. Lam, R. Wilcoxon, and N. Lower, "On the potential of galinstan-based minichannel and minigap cooling," *IEEE Trans Compon Packaging Manuf Technol*, vol. 4, no. 1, 2014, doi: 10.1109/TCPMT.2013.2274699.

[46] Y. Xie, D. Deng, G. Pi, X. Huang, and C. Zhao, "Fabrication of silicon carbide microchannels by thin diamond wheel grinding," *International Journal of Advanced Manufacturing Technology*, vol. 111, no. 1–2, 2020, doi: 10.1007/s00170-020-06085-0.

[47] R. Prasher, "Nano and Micro Technology-Based Next-Generation Package-Level Cooling Solutions," *Intel Technology Journal*, vol. 09, no. 04, 2005, doi: 10.1535/itj.0904.03.

[48] H. Y. Zhang, D. Pinjala, T. N. Wong, K. C. Toh, and Y. K. Joshi, "Single-phase liquid cooled microchannel heat sink for electronic packages," *Appl Therm Eng*, vol. 25, no. 10, 2005, doi: 10.1016/j.applthermaleng.2004.09.014.

[49] J. P. Calame, R. E. Myers, S. C. Binari, F. N. Wood, and M. Garven, "Experimental investigation of microchannel coolers for the high heat flux thermal management of GaN-on-SiC semiconductor devices," *Int J Heat Mass Transf*, vol. 50, no. 23–24, 2007, doi: 10.1016/j.ijheatmasstransfer.2007.03.013.

[50] D. Nayak, L. T. Hwang, I. Turlik, and A. Reisman, "A high-performance thermal module for computer packaging," *J Electron Mater*, vol. 16, no. 5, 1987, doi: 10.1007/BF02657911.

[51] V. Manoj Siva, A. Pattamatta, and S. K. Das, "Effect of flow maldistribution on the thermal performance of parallel microchannel cooling systems," *Int J Heat Mass Transf*, vol. 73, 2014, doi: 10.1016/j.ijheatmasstransfer.2014.02.017.

[52] B. Atkinson, M. P. Brocklebank, C. C. H. Card, and J. M. Smith, "Low Reynolds number developing flows," *AIChE Journal*, vol. 15, no. 4, 1969, doi: 10.1002/aic.690150414.

[53] C. L. Wiginton and C. Dalton, "Incompressible laminar flow in the entrance region of a rectangular duct," *Journal of Applied Mechanics, Transactions ASME*, vol. 37, no. 3, 1970, doi: 10.1115/1.3408620.

[54] R. W. Keyes, "Heat Transfer in Forced Convection Through Fins," *IEEE Trans Electron Devices*, vol. 31, no. 9, 1984, doi: 10.1109/T-ED.1984.21691.

[55] A. Weisberg, H. H. Bau, and J. N. Zemel, "Analysis of microchannels for integrated cooling," *Int J Heat Mass Transf*, vol. 35, no. 10, 1992, doi: 10.1016/0017-9310(92)90089-B.

[56] J. P. Calame, R. E. Myres, F. N. Wood, and S. C. Binari, “Simulations of direct-die-attached microchannel coolers for the thermal management of GaN-on-SiC microwave amplifiers,” *IEEE Transactions on Components and Packaging Technologies*, vol. 28, no. 4, 2005, doi: 10.1109/TCAPT.2005.848584.

[57] A. G. Fedorov and R. Viskanta, “Three-dimensional conjugate heat transfer in the microchannel heat sink for electronic packaging,” *Int J Heat Mass Transf*, vol. 43, no. 3, 2000, doi: 10.1016/S0017-9310(99)00151-9.

[58] S. G. Kandlikar and W. J. Grande, “Evaluation of single phase flow in microchannels for high heat flux chip cooling-thermohydraulic performance enhancement and fabrication technology,” *Heat Transfer Engineering*, vol. 25, no. 8. 2004. doi: 10.1080/01457630490519772.

[59] A. Dewan and P. Srivastava, “A review of heat transfer enhancement through flow distribution in a microchannel,” *Journal of Thermal Science*, vol. 24, pp. 203–214, 2015.

[60] B. E. Burk, T. P. Grumstrup, T. A. Bevis, J. Kotovsky, and T. M. Bandhauer, “Computational examination of two-phase microchannel heat transfer correlations with conjugate heat spreading,” *Int J Heat Mass Transf*, vol. 132, pp. 68–79, Apr. 2019.

[61] C. Anderson, J. Richey, M. Fish, and T. Bandhauer, “Peak Temperature Mitigation of a Multimicrochannel Evaporator Under Transient Heat Loads,” *Journal of Electronic Packaging, Transactions of the ASME*, vol. 143, no. 4, 2021, doi: 10.1115/1.4052360.